Lymphangiogenesis driven by VEGF-C reshapes tumor immune landscape and enables tumor eradication by viral immunotherapy

Ruben Fernandez-Rodriguez[1,2,3]†, Sara Cuadrado-Castano[4,6,7]†, Andrew Edwards[1,2,3], Anita Rogic[1,2,3], Yonina Bykov[4], Ignacio Mena[4,5], Noelia Dasilva-Freire[4], Alice O Kamphorst[2,3,7], Rosa Karlic[8], Amir Horowitz[2,3,7], Adolfo García-Sastre[3,4,5,6, 9,10], Mihaela Skobe[1,2,3]*

[1]Laboratory of Cancer Lymphangiogenesis, Icahn School of Medicine at Mount Sinai, New York, NY, USA;
[2]Department of Oncological Sciences, Icahn School of Medicine at Mount Sinai; New York, NY, USA;
[3]Tisch Cancer Institute, Icahn School of Medicine at Mount Sinai; New York, NY, USA;
[4]Department of Microbiology, Icahn School of Medicine at Mount Sinai; New York, NY, USA;
[5]Global Health and Emerging Pathogens Institute, Icahn School of Medicine at Mount Sinai; New York, NY, USA;
[6]Icahn Genomics Institute (IGI), Icahn School of Medicine at Mount Sinai; New York, NY, USA;
[7]Precision Immunology Institute (PrIISM), Icahn School of Medicine at Mount Sinai; New York, NY, USA;
[8]Bioinformatics group, Division of Molecular Biology, Department of Biology, Faculty of Science, University of Zagreb; Zagreb, Croatia;
[9]Division of Infectious Diseases, Department of Medicine, Icahn School of Medicine at Mount Sinai; New York, NY, USA;
[10]Department of Pathology, Molecular and Cell-Based Medicine, Icahn School of Medicine at Mount Sinai; New York, NY, USA.

*Corresponding author, e-mail: mihaela.skobe@mssm.edu

†These authors contributed equally to this work.

Short Title: VEGF-C, lymphatics and APMV viral immunotherapy

ABSTRACT

Vascular Endothelial Growth Factor C (VEGF-C) is a key lymphangiogenic growth factor expressed by many types of cancer. Here, we investigated the effects of tumor-derived VEGF-C on the therapeutic efficacy of oncolytic virotherapy with avian paramyxoviruses APMV-1 (NDV) and AMPV-4. Treatment of B16F10 tumors not expressing VEGF-C with either virus led to tumor growth delay, and complete responses were rare. In contrast, when tumors expressed VEGF-C, viral therapy led to complete remission and long-term immunological memory in most mice. Upon re-challenge, most mice remained tumor- and metastasis-free for over 18 months, indicating durable immunity. VEGF-C induced tumor lymphangiogenesis, which correlated with high $CD8^+$ and $CD4^+$ T-cell densities in proximity of lymphatic vessels. Spectral flow cytometry revealed distinct changes in the composition and activation of $CD8^+$, $CD4^+$ T cells and NK cells associated with complete remission. In responders, tumors were highly enriched in $CD8^+CD25^+$ PD-1^+ effector T cells. Composition of T cells was altered in sentinel and in contralateral lymph nodes, indicating a systemic immune response. Taken together, these data demonstrate VEGF-C-induced changes in tumor immune landscape which are critical for achieving complete response and support combining VEGF-C with APMV virotherapy as a novel highly effective strategy for cancer treatment.

54 **INTRODUCTION**

55 Viral immunotherapy is an emerging cancer treatment that leverages the ability of certain viruses to break
56 immune tolerance and stimulate anti-tumor immunity (*1*). A major challenge in clinical development of
57 oncolytic viruses (OVs) has been their limited therapeutic efficacy as monotherapy, often leading to partial
58 responses (*2*). Consequently, OVs are mainly employed in combination with immune checkpoint
59 inhibitors, chemotherapy, or radiotherapy, to enhance therapeutic efficacy (*3*), and various strategies
60 have been explored to enhance immune activation by OVs that directly target immune cells (*4-7*). To
61 date, four OVs have been approved worldwide for cancer treatment (*1, 8-11*). These promising results in
62 the clinic highlight the therapeutic potential of OVs as well as the need for novel strategies that improve
63 efficacy while minimizing toxicity.

64

65 Avian avulaviruses, referred to as avian paramyxoviruses (APMVs) are negative-sense single-stranded
66 RNA (ssRNA (-)) viruses (*12*) with oncolytic activity, strong immunostimulatory properties and an
67 excellent safety profile (*6, 13-15*). Among them, Newcastle disease virus (NDV; APMV-1) has been most
68 extensively studied and has garnered significant interest for cancer therapy (*14, 16-21*). APMVs
69 preferentially replicate in tumor cells, exploiting their defective antiviral defenses (*1*). Their replication is
70 restricted to the cytoplasm of the host cell, without DNA intermediates (*12*), which minimizes the risk of
71 genomic integration and enhances safety. Importantly, APMVs are not human pathogens (*22*). Given
72 their strong safety profile, inherent selectivity for cancer cells, and ability to elicit potent anti-tumor
73 immunity APMVs demonstrate strong potential as cancer therapeutics.

74 Enhancing the anti-tumor efficacy of OVs requires a deeper understanding of the key determinants of
75 immune response within the tumor microenvironment (TME), and much attention has been given to the
76 interactions between tumor cells and various immune cell subsets. Tumor vasculature also plays an
77 important role in shaping TME, and recently lymphatic vessels have emerged as modulators of immunity
78 (*23-25*). Beyond serving as conduits for immune cell trafficking to the lymph nodes, they actively shape

immune responses through chemokine production, scavenger functions, and antigen presentation among others (*26*). Lymphatics can promote both tolerance and immunity, and their impact is highly context dependent. Vascular Endothelial Growth Factor C (VEGF-C) is a key lymphangiogenesis factor (*27-29*), which activates lymphatic endothelial cells (LECs) through the tyrosine kinase receptors VEGFR-3 (*27, 30-33*) and VEGFR-2 (*27*). While initially preclinical studies demonstrated that VEGF-C activation of VEGFR-3 promotes an immunosuppressive microenvironment in tumors, more recent studies indicate that VEGF-C potentiates immunotherapy response (*34, 35*). These seemingly contradictory outcomes underscore the context-dependent influence of VEGF-C and lymphatics on tumor immunity.

Here, we investigate the effects of VEGF-C on therapeutic efficacy of APMVs in mouse melanoma. We show that VEGF-C markedly enhances anti-tumor immune responses induced by APMVs. Characterization of tumor immune landscape demonstrates unique changes of immune cell subsets in B16F10 tumors expressing VEGF-C and treated with APMV-1 (NDV), that were associated with complete response. This study demonstrates that VEGF-C potently enhances the effects of OVs leading to durable anti-tumor response and immunological memory.

RESULTS

Oncolytic viral therapy with APMVs leads to complete remission of B16F10 tumors expressing VEGF-C

We used NDV and APMV-4 to examine their effectiveness against tumors expressing VEGF-C (*5, 21, 36*). We generated B16F10 melanoma to constitutively express mouse VEGF-C (B16/VEGF-C) and VEGF-C expression was confirmed in vitro by qPCR, ELISA, Western Blot, and by immunostaining (Fig. 1a-c, Suppl. Fig. 1a-b). B16/VEGF-C cells secreted 33 kDa VEGF-C protein, which binds VEGFR-3 but not VEGFR-2 (*29, 30*) (Fig. 1c). B16/EV cells, transduced with an empty vector (B16/EV) showed no detectable expression of VEGF-C mRNA or protein (Fig. 1a-c, Suppl. Fig. 1a-b).

104

105 B16/VEGF-C and B16/EV tumors (~50mm^3) were treated with NDV or APMV-4 by intratumoral injection
106 every two days, for four doses total (1x10^7 PFU each) (Fig. 1d). NDV delayed B16/EV tumor growth (5/7),
107 with 14% mice in complete remission (1/7), while triggering complete remission in 87% of mice with
108 B16/VEGF-C tumors (6/7) (Fig. 1e). APMV-4 treatment of B16/EV tumors also significantly delayed tumor
109 growth (5/7), but did not induce CR. However, when tumors expressed VEGF-C, APMV-4 treatment led
110 to complete remission in 100% of the mice (7/7) (Fig. 1e). We observed a transient increase in tumor
111 volume after two treatments, prior to tumor regression (Fig. 1e). This is consistent with the previous
112 studies of immune checkpoint inhibition and has been correlated with immune cell infiltration and
113 inflammation (*15*). Tumors regressed rapidly; by day eight following treatment with APMV-4 or NDV, 71%
114 of tumors had fully regressed (Fig. 1f). Mice were monitored post-treatment with either NDV or APMV-4
115 for up to 2 years and 4 months (843 days), during which no tumor recurrence was observed, indicating
116 complete tumor eradication (Fig. 1g, Table 1). Cumulative data from eight independent experiments show
117 that APMV-4 is highly effective on tumors expressing VEGF-C, leading to complete remission (CR) in
118 86% of mice (n=49), compared to 0% CR when VEGF-C was not present (n=17) (Fig. 1h, Table 1).
119 APMV-4 was more efficient in eliminating B16/VEGF-C tumors than NDV (86% vs. 71%, respectively)
120 (Fig. 1h, Table 1).

121

122 **Surviving mice are metastasis free and protected from tumor development upon re-challenge**

123 To assess the durability of response to NDV or APMV-4 therapy, mice in complete remission (CR) were
124 re-challenged with B16/EV tumor cells 90 days post-treatment, by injecting tumor cells into the
125 contralateral flank. As expected, naïve control mice rapidly developed tumors, reaching maximum size
126 within 20 days (Fig. 1i). In contrast, most mice in CR were protected from developing tumors after re-
127 challenge and remained tumor-free during the observation period of up to 546 days (~18 months) (Fig.
128 1i, j, Table 1). Mice frequently displayed vitiligo at tumor rejection sites, consistent with local immune
129 activation (Fig. 1j), as reported previously for checkpoint blockade (*37*). Cumulative protection rates post

130 re-challenge were 69% (n=13) in APMV-4 and 58% (n=12) in NDV-treated group (Fig. 1h, Table 1). These
131 findings demonstrate that NDV and APMV-4 treatments consistently induce robust and sustained anti-
132 tumor immunity when VEGF-C is present in tumors.
133
134 To assess effects of APMV-4 treatment on metastases, we immunostained lymph nodes from B16/VEGF-
135 C tumor-bearing mice for MelanA (Fig. 1k-o, Table 2). By day 21 after tumor inoculation, all mice in control
136 group developed macrometastases in sentinel LNs (Fig. 1k). Strikingly, in sentinel LNs of APMV-4-treated
137 mice metastases were not detectable for the entire observation period, ranging from 4-18 months (Fig.
138 1k-o, Table 2). These results demonstrate that APMV-4 treatment of B16 tumors expressing VEGF-C
139 eliminates lymph node metastases, indicating that metastasis-promoting effects of VEGF-C can be
140 reversed in the context of immune activation, such as during viral therapy.
141
142 **VEGF-C-expressing tumors are enriched in T cells**
143 To assess the effects of VEGF-C on the tumor microenvironment, we carried out immunostaining for
144 lymphatic and blood vasculature, as well as for the key immune cell subsets (Fig. 2a). Tumors were
145 collected 12h after the second treatment, when tumor sizes were comparable across all treatment groups,
146 and just prior to the onset of regression (Suppl. Fig. 2a).
147 B16/EV tumors did not express VEGF-C (Fig. 1a-c) and showed no intratumoral or peritumoral
148 lymphangiogenesis, as indicated by LYVE-1 staining (Fig. 2a, b). NDV-treated B16/EV tumors similarly
149 lacked lymphatics in or around the tumors (Fig. 2a, b). In contrast, VEGF-C expression induced tumor
150 lymphangiogenesis, as expected (Fig. 2a, b), with higher lymphatic densities at the tumor periphery than
151 in the center, and comparable distribution in PBS- and NDV-treated B16/VEGF-C tumors (Fig. 2a, b).
152 VEGF-C also promoted lymphangiogenesis and dilation of lymphatics in overlying skin, while in the skin
153 adjacent to B16/EV tumors, lymphatics appeared normal in density and morphology (Suppl. Fig. 2b).
154 NDV treatment alone did not induce lymphangiogenesis or alter the appearance of lymphatics in tumors

155 or skin within 2.5 days from the onset of treatment (Fig. 2a, b; Suppl. Fig. 2). Angiogenesis was not
156 induced by VEGF-C. However, NDV decreased blood vessel area in tumors by decreasing both, their
157 size and density (Fig. 2a, b).

158 VEGF-C markedly increased $CD45^+$ cells in tumors, whereas NDV did not within 2.5 days from the onset
159 of treatment (Fig. 2a, b; Suppl. Fig. 2). Moreover, VEGF-C expression was associated with high densities
160 of $CD8^+$ and $CD4^+$ T-cells in tumors, while VEGF-C-negative tumors were nearly devoid of T cells at this
161 time-point (Fig. 2a, b; Suppl. Fig. 2c). Densities of $F4/80^+$ macrophages were high across all groups, with
162 no changes due to VEGF-C or NDV (Fig. 2a, b). Conversely, $Ly6G^+$ neutrophils were present
163 peritumorally, but absent within tumors across all treatment groups (Suppl. Fig. 2c).

164 VEGFR-3, the key VEGF-C receptor, was detected on all LYVE-1^+ lymphatic vessels in B16/VEGF-C
165 tumors by immunostaining (Suppl. Fig. 3), with no VEGFR-3 detected on other cell types, and no changes
166 in the levels or pattern of VEGFR-3 expression upon NDV treatment (Suppl. Fig. 3). Taken together,
167 these findings demonstrate a positive correlation between lymphangiogenesis and T-cell densities and
168 suggest that VEGF-C promotes T cell expansion indirectly, by activating VEGFR-3 signaling on lymphatic
169 endothelial cells (LECs).

170

171 **Immune profiling of tumors reveals unique changes of immune cell composition associated with**
172 **complete response.**

173 To investigate mechanisms underlying tumor growth delay (EV/NDV) or complete regression (VEGF-
174 C/NDV), we profiled immune cell phenotypes and activation states in the tumor microenvironment. High-
175 dimensional spectral flow cytometry was performed on tumors collected 12h after the second NDV
176 treatment (Suppl. Fig. 2a), using markers for myeloid and lymphoid lineages (Table 3, Panel 1). Given
177 the high complete response (CR) rate in B16VEGF-C/NDV-treated animals (71%), changes in immune
178 cell subsets could be linked to tumor regression with high confidence.

179 Analysis of B16/VEGF-C NDV-treated tumors by manual gating showed an increase in relative
180 frequencies of $CD4^+$ and $CD8^+$ T cells, and a decrease in dendritic cells (DCs), monocytes and B cells
181 associated with CR (Fig. 2c-e; Suppl. Fig. 4). $CD103^+$ DCs, which are a key antigen-presenting cells
182 (APCs) priming tumor-specific CD8+ T cells(*38*), as well as $CD11b^+$ DCs, showed reduced frequencies
183 only in NDV-treated B16/VEGF-C tumors (Fig. 2c-e, Suppl. Fig. 5a). These findings suggest enhanced
184 DC mobilization to LNs following NDV treatment of VEGF-C-expressing tumors, which is consistent with
185 the previous study demonstrating that mobilizing DCs improved NDV-based virotherapy against B cell
186 lymphoma (*39*).
187
188 NDV treatment of B16/EV tumors, which induced partial tumor regression, increased monocyte and
189 neutrophil frequences compared to PBS controls (Fig. 2d, e; Suppl. Fig. 5a). Neutrophils were localized
190 almost exclusively at the tumor periphery, as demonstrated by immunostaining (Supp. Fig. 5b). NDV
191 treatment of both B16/EV and B16/VEGF-C tumors showed a trend toward increased NK cell frequencies
192 compared to PBS controls, but it was not statistically significant, likely due to the low NK cell abundance
193 relative to other immune cell subtypes (Fig. 2d, e; Suppl. Fig. 5a). These data highlight several key
194 differences in immune cell composition in response to NDV treatment, depending on the presence or
195 absence of VEGF-C.
196
197 **VEGF-C and NDV cooperate to shift the tumor immune landscape toward effector $CD8^+$ T cells**
198 Given the increase in $CD8^+$ and $CD4^+$ T cells in VEGF-C-expressing tumors, we analyzed T cell
199 phenotypes associated with partial and complete anti-tumor responses. Analysis of T-cell surface
200 markers (Table 3, Panel 2) by manual gating revealed a significant increase in $CD25^+PD\text{-}1^+CD8^+$ T cells
201 in VEGF-C/NDV tumors, correlating with complete response (Fig. 3a, b). VEGF-C alone also increased
202 this subset, while NDV showed a trend (Fig. 3b). In contrast, $CD44^+PD\text{-}1^+CD8^+$ T cell frequences were
203 not significantly changed across conditions (Fig. 3c, Suppl. Fig. 6a), highlighting CD25 as a distinguishing

204 marker associated with CR. $CD25^+CD8^+$ T cells were mainly expanded by NDV, and this was further
205 enhanced by VEGF-C (Suppl. Fig. 6b-e). VEGF-C, however, strongly increased PD-1 expression on this
206 subset (Suppl. Fig. 6f, g). All $CD8^+CD25^+$ T cells expressed $CD44^+$, suggesting that they are Ag-
207 experienced (Suppl. Fig. 6h). There was in increase in CTLA-4^+ $CD8^+CD25^+$PD-1^+ T cells upon NDV
208 treatment, but they lacked TIM-3 (Fig. 3d). Notably, frequencies of $CD4^+Foxp3^+$ Tregs were significantly
209 decreased and the ratio of $CD25^+$PD-1^+CD8^+ T cells to Tregs was increased only in VEGF-C/NDV tumors
210 (Fig. 3e, f). Taken together, these data demonstrate robust expansion of $CD25^+$PD-1^+ effector $CD8^+$ T
211 cells and reduction of Tregs selectively in NDV-treated B16/VEGF-C tumors, suggesting a key role of
212 these subsets in tumor eradication.
213
214 VEGF-C exhibited potent effects on $CD4^+$ T cells. VEGF-C increased frequencies of naïve $CD4^+$ T cells
215 ($CD62L^+CD44^-$) (Fig. 3g), but it reduced $CD62L^+CD44^+$ $CD4^+$ T cells, which were abundant in B16F10
216 tumors, and expanded with NDV (Fig. 3h). In untreated tumors, $CD62L^+CD44^+$ $CD4^+$ T cells were positive
217 for CD25, CTLA-4, and KLRG1, and this population was increased in frequencies with NDV (Fig. 3h, i).
218 However, in VEGF-C expressing tumors, CD25, CTLA-4, and KLRG-1 were significantly reduced on
219 $CD62L^+CD44^+$ $CD4^+$ T cells (Fig. 3i), suggesting reduced sensitivity to IL-2 and reduced inhibitory
220 signaling. VEGF-C also markedly decreased $CD62L^-CD44^+$CTLA-4^+ $CD4^+$ T cells (Fig. 3l). It also
221 increased KLRG1^+ subset, but did not change PD-1 across conditions (Fig. 3l). Either NDV or VEGF-C
222 alone reduced frequences of $CD25^+CD62L^-CD44^+$ $CD4^+$ T cells (Fig. 3l), whereas VEGF-C potently
223 decreased CTLA-4^+CD25^+ subset (Fig. 3m). Decrease in CTLA-4^+CD25^+ $CD4^+$ T cell subsets, likely
224 Tregs, suggests reduced capacity of these cells to suppress immune responses.
225
226 Unsupervised bioinformatic analysis separately identified three $CD8^+$ T cell clusters with significantly
227 changed frequences in VEGF-C/NDV group compared to EV/NDV. Specifically, effector $CD8^+$ T cell
228 clusters 7 and 16, both $CD28^+CD44^+$PD-1^+, were the most enriched populations, whereas $CD8^+$ T cell
229 cluster 1 ($CD28^+CD44^+$ CTLA-4^+TIM-3^+), likely early exhausted cells, were decreased (Fig. 3 n, o; Suppl.

230 Fig. 7). Effector $CD8^+$ T cell cluster 7 was also the most abundant of all CD8 clusters affected by treatment
231 (Fig. 3n, o). The number of $CD4^+$ T cells affected by treatments was approximately double that of $CD8^+$
232 T cells (CD4:CD8 ratio = 2.18:1). $CD4^+$ T cell clusters decreased with NDV/VEGF-C were all CTLA-4^+;
233 (Cluster 4 and 12, $CD44^+CD28^+$CTLA-4^+) and Cluster 1 ($CD44^+CD28^+$CTLA-4^+PD-1^+TIM-3^+). Cluster 1
234 was most abundant $CD4^+$ T cell subset among those affected by treatment. Taken together, VEGF-C
235 and NDV combined drive a strong anti-tumor immune response by reducing immunosuppressive or
236 exhausted cells and expanding effector T cells. Since VEGF-C alone increases total $CD8^+$ T cells, this
237 results in increased total T cell effectors in VEGF-C/NDV tumors, correlating with tumor eradication.
238
239 **T cells and NK cells are highly activated in VEGF-C-expressing tumors treated with NDV**
240 We next analyzed the activation status of NK, $CD8^+$, and conventional $CD4^+$ T cells, by assessing the
241 expression of IFNγ, TNFα and granzyme B (GzmB) using spectral flow cytometry (Table 3, Panel 3).
242 Manual gating revealed strong activation of NK and $CD8^+$ T cells, with NK cells showing very high
243 activation levels (Fig. 4a. b, Suppl. Fig. 8b-d). NDV markedly increased IFNγ^+ NK cells in tumors and this
244 was further enhanced by VEGF-C (Fig. 4b). NDV also triggered a 10-fold increase in GzmB$^+$ NK cells
245 independent of VEGF-C, indicating enhanced cytotoxic capacity of NK cells. Conversely, VEGF-C, but
246 not NDV, increased TNFα^+ NK cells (Fig. 4b), most of which co-expressed IFNγ^+ (Suppl. Fig. 7d).
247
248 $CD8^+$GrB$^+$ T cells, which are potent cytotoxic T cells, were significantly increased only in VEGF-C/NDV
249 tumors (Fig. 4c). VEGF-C increased TNFα^+ $CD8^+$ T cells which were also IFNγ^+ (Fig. 4c, Suppl. Fig. 8d),
250 while NDV alone had no effect on $CD8^+$ T cell activation at the time-point examined (Fig. 4c).
251 Conventional $CD4^+$ T cells in VEGF-C/NDV tumors showed an NDV-driven increase in GzmB, and a
252 decrease in IFNγ^+ and TNFα^+ $CD4^+$ T cells (Fig. 4d, Suppl. Fig. 8d). Taken together, these data
253 demonstrate enhanced activation of NK, $CD8^+$ and $CD4^+$ T cells in NDV-treated VEGF-C-expressing
254 tumors, correlating with complete response.
255

256 Analysis of the proportional abundance of activated CD45$^+$ cells demonstrated that NDV treatment mainly
257 activated NK cells, as indicated by IFNγ and GzmB expression. In the presence of VEGF-C, however,
258 the ratio of activated CD8$^+$ T cells to NK cells increased in NDV-treated tumors (Fig. 4e, Suppl. Fig. 8e,
259 f). VEGF-C alone had minimal or no impact on proportions of activated cells in untreated tumors (Suppl.
260 Fig. 8e, f), consistent with the observation that VEGF-C had no anti-tumor effects in the absence of
261 immune activation with the virus. Finally, relative proportion of activated effector cells among all CD45+
262 cells increased ~5-fold in VEGF-C/NDV tumors and ~2-fold in untreated B16/VEGF-C tumors (Fig. 4f).
263 Together, these data demonstrate a marked accumulation of activated effector cells, particularly CD8$^+$ T
264 cells, in VEGF-C/NDV tumors.
265
266 Unsupervised bioinformatic analysis separately identified six clusters of T cell and NK cell populations
267 with distinct expression patterns of effector molecules, including three clusters of polyfunctional T cells
268 (Fig. 4g-i, Suppl. Fig. 8g). Four CD8$^+$ T cell, one CD4$^+$ T cell and one NK cell cluster displayed enhanced
269 production of GgzmB, IFNγ and/or TNFα. Notably, all six clusters were significantly expanded in VEGF-
270 C/NDV group compared to EV/NDV (Fig. 4g-i). In summary, these data show that NDV combined with
271 VEGF-C strongly activates CD8$^+$ T cells, conventional CD4$^+$ T cells and NK cells, and that the expansion
272 of activated effector cells is linked to tumor eradication.
273
274 **T cells establish close contact with tumor lymphatic endothelium**
275 We observed expansion of T-cell compartment in VEGF-C expressing tumors, with maximal activation
276 following NDV treatment in the presence of VEGF-C. To better understand the spatial relationship
277 between lymphatics and T cells, we performed immunostaining on B16/VEGF-C tumor samples collected
278 12h following the second dose of NDV treatment (Fig. 5). High lymphatic vessel densities in tumors
279 correlated with high CD8$^+$ and CD4$^+$ T cell densities (Fig 5a-j). Analysis of lymphatic vessel distribution
280 demonstrated that lymphatic densities were high at the tumor periphery (Fig. 5a, f) and sparse in the
281 tumor center (Fig. 5c, h). Accordingly, T cell densities were high at the tumor periphery, and sparse in

282 the tumor center, mirroring lymphatic vessel distribution (Fig. 5a-j). Most T cells localized near lymphatics,
283 suggesting direct interaction with tumor LECs (Fig. 5k), and z-stack confocal microscopy and
284 fluorescence intensity analysis confirmed direct contact between $CD8^+$ T cells and LECs (Fig. 5l, m).
285
286 Proximity analysis revealed that the majority of $CD8^+$ T cells in tumors were in close proximity to
287 lymphatics, irrespective of NDV treatment (Fig. 5n-s). As many as 50% of $CD8^+$ T cells were in direct
288 contact with LECs (Fig. 5q) and ~65% within a 50 µm perimeter of lymphatic vessels (Fig. 5s). $CD4^+$ T
289 cells showed even closer association with lymphatics, with ~75% in direct contact with LECs (Fig. 5p-s).
290 NDV treatment did not affect localization of $CD8^+$ T or $CD4^+$ T cells relative to lymphatics (Fig. 5p-s).
291 These data demonstrate that T cells in VEGF-C expressing tumors establish direct contact with LECs.
292
293 **Distinct changes in T-cell composition of sentinel and distant lymph nodes are associated with**
294 **complete response**
295 To assess changes in the immune composition of lymph nodes (LNs), we next analyzed tumor sentinel
296 (sLN) and contralateral, non-sentinel lymph nodes (nsLN) by spectral flow cytometry (Fig. 6). LNs were
297 collected 12h after the second NDV or PBS treatment of B16/EV and B16/VEGF-C tumors (Suppl. Fig.
298 9a). In sentinel LNs, relative frequences of total $CD8^+$ T cells decreased upon NDV treatment of
299 B16/VEGF-C tumors only, whereas total $CD4^+$ T cell frequences remained unchanged across treatment
300 groups (Fig. 6a, b, Suppl. Fig. 9b). Naïve $CD8^+$ T cells ($CD62^{hi}CD44^{low}$) were markedly reduced by NDV,
301 VEGF-C, or their combination (Fig. 6c, Suppl. Fig. 9c). Both, CM ($CD62L^{hi}CD44^{hi}$) and EM
302 ($CD62L^{low}CD44^{hi}$) T cells were reduced only when B16/VEGF-C tumors were treated with NDV (Suppl.
303 Fig. 9c-e). $CD62L^{low}CD44^{low}$ $CD8^+$ T cells were enriched in sLNs of both, EV/NDV and VEGF-C/NDV
304 tumors (Fig. 6d, Suppl. Fig. 9c). In contralateral non-sentinel LNs, $CD8^+$ T cell subsets showed similar
305 but less pronounced changes than in sentinel LNs following NDV treatment of B16/VEGF-C tumors; most
306 notably, reduced total and naïve $CD8^+$ T cells and increased $CD62^{low}CD44^{low}$ $CD8^+$ T cells (Fig. 6a, c, d,
307 Suppl. Fig. 9c).

308

309 Changes in $CD4^+$ T cell subsets in sentinel LNs paralleled those of $CD8^+$ T cells (Fig. 6e, Suppl. Fig. 9).
310 Naïve $CD4^+$ T cells were markedly reduced by NDV, VEGF-C, or their combination (Fig. 6e). Conversely,
311 $CD62^{low}CD44^{low}$ $CD4^+$ T cells were highly enriched upon NDV treatment, independent of VEGF-C (Fig.
312 6f). $CD4^+$ CM and EM frequences remained unchanged (Suppl. Fig. 9 f-h). Of note, NDV triggered stark
313 decrease in conventional $CD4^+$ T cells and an increase in Tregs in sLNs, especially in combination with
314 VEGF-C (Fig. 6g, h; Suppl. Fig. 9i). In the nsLNs, CD4 T cell changes resembled those seen in sentinel
315 LNs but were less pronounced. Specifically, NDV/VEGF-C combination decreased frequencies of naïve
316 and conventional $CD4^+$ T cells, and increased frequencies of $CD62^{low}CD44^{low}$ $CD4^+$ T cells and Tregs
317 (Fig. 6e-h).

318

319 We next performed unsupervised analysis of spectral flow cytometry data from lymph nodes. NDV
320 treatment of B16F10/VEGF-C tumors induced T cell responses in both sLNs and nsLNs, characterized
321 by the dominant emergence of several $CD8^+$ and $CD4^+$ T cell clusters, along with selective depletion or
322 marked reduction of others (Fig. 6i-l). Top three enriched $CD8^+$ T cell clusters were all positive for Ly6C
323 and likely represent recently activated effector $CD8^+$ T cells (Cl. 1 and 3, $CD44^+Ly6C^+$; Cl. 2,
324 $CD103^+Ly6C^+$). This response was particularly striking in nsLNs, where multiple $CD8^+$ and $CD4^+$ T cell
325 subsets selectively expanded, while several others were markedly reduced. These data demonstrate that
326 NDV and VEGF-C induce changes in both sentinel and in distant LNs, suggesting the importance of
327 systemic effects in achieving tumor elimination.

328
329
330 **VEGF-C is widely expressed in human cancers**

331 We next evaluated VEGF-C mRNA expression across 31 human cancer types by analyzing bulk RNA-
332 seq data from the TCGA Pan-Cancer Atlas (PANCAN) (Fig. 7). VEGF-C was expressed in all solid
333 tumor types analyzed, and it was highly expressed in 47.7% of all tumor samples in the database,

334 where high expression is defined as $\log_2$(TPMK) $\geq$ 7, corresponding to the median value across all
335 tumors (Fig. 7a). High VEGF-C expression was observed in 13 tumor types, including bladder cancer
336 (BLCA), breast cancer (BRCA), head and neck cancer (HNSC), kidney cancer (KICH, KIRC), lung
337 adenocarcinoma (LUAD), mesothelioma (MESO), pancreatic adenocarcinoma (PAAD), neuroendocrine
338 tumors (PCPG), sarcoma (SARC), and thyroid cancer (THCA) (Fig. 7a). Notably, 100% of thyroid
339 cancers (THCA), 80% of sarcomas (SARC), 79% of pancreatic cancers (PAAD) and 65% of head and
340 neck cancers (HNSC) exhibited high VEGF-C expression (Fig. 7b). In contrast, glioblastoma multiforme
341 (GBM), low-grade glioma (LGG), and adenocarcinomas of the colon and rectum (COAD, READ), were
342 among the lowest VEGF-C-expressing tumors (Fig. 7a, b). In cutaneous and uveal melanomas (SKCM,
343 UVM) VEGF-C expression was ubiquitous with intermediate expression levels. These findings highlight
344 a subset of tumors with high VEGF-C expression, suggesting that they may be more amenable to
345 APMV-based virotherapy.
346

347 **DISCUSSION**
348

349 Our results demonstrate exceptional anti-tumor efficacy of APMV-based viral immunotherapies in
350 presence of VEGF-C in tumors. Treatment of B16F10 tumors with either NDV or APMV-4 oncolytic
351 viruses led to complete remission in most animals when tumors expressed VEGF-C. Responses were
352 durable, with long-term survival, protection from tumor development upon re-challenge, and absence of
353 metastases, indicating the establishment of robust immunological memory. These results identify a
354 combination of APMV and VEGF-C as a highly effective anti-tumor therapeutic approach leading to
355 durable responses and highlight a novel strategy for improving efficacy of oncolytic viruses by activating
356 the lymphatic system.
357 It is important to emphasize that we show exceptional anti-tumor efficacy of APMVs as a monotherapy.
358 OVs generally show limited efficacy as a single agent and primarily delay tumor progression(*11, 15, 40*).
359 NDV, for example, has been shown to impair tumor growth and prolong survival across multiple studies,

360 but it rarely leads to tumor eradication(*4-6, 15, 36, 40*). Most current strategies for improving efficacy of
361 OVs focus on enhancing anti-tumor immune responses by targeting immune cells directly. These
362 approaches typically involve engineering viruses to express immunostimulatory cytokines, superagonists
363 for co-stimulation, or combining OVs with systemic immunotherapies such as anti-PD-1 or anti-CTLA-
364 4(*4-7, 21, 41-43*) and often require concurrent delivery of multiple immunomodulators to achieve robust
365 therapeutic outcomes. For example, NDV expressing IL-12, CD28 superagonist, and systemic PD-1
366 blockade achieved 37% complete response in a mouse model(*21*), whereas achieving complete
367 response rates greater than 70% required combining NDV concurrently with blocking antibodies against
368 PD-1, PD-L1, and CTLA-4(*18, 40*). NDV treatment with anti-PD-1 alone led to only 20% CR in B16F10
369 model(*4, 5*).
370
371 In striking contrast, we observed complete response (CR) rates exceeding 90% using NDV or APMV-4
372 as single-agent therapy in VEGF-C-expressing tumors, without any additional immunomodulatory agents.
373 These findings underscore the central role of VEGF-C and lymphatics in orchestrating anti-tumor
374 immunity. Seminal work by Fankhauser and Swartz (2017) first demonstrated that VEGF-C-mediated
375 lymphangiogenesis can enhance immunotherapy efficacy in preclinical models of melanoma(*34*). Several
376 immunotherapy strategies including adoptive T cell transfer, DC vaccination, and CpG adjuvant have
377 shown prolonged survival and 10-20% CR using B16F10/VEGF-C tumors, but only in the presence of a
378 potent model antigen(*34*). Cancer vaccine using irradiated tumor cells engineered to secrete VEGF-C
379 (VEGF-C vax) conferred prophylactic protection against melanoma and improved responses when
380 combined with immune checkpoint blockade, but did not induce complete remission(*35*). Similarly,
381 prophylactic delivery of AAV-VEGF-C protected against glioblastoma (GBM) development(*44*). In
382 therapeutic setting however, PD-1 blockade combined with VEGF-C achieved high CR rates only when
383 GBM tumor burden was low, while in established tumors, dual PD-1 and TIM-3 blockade was necessary
384 to extend survival but did not induce CR(*44*).

385 A key distinction of our study is the exceptionally high survival benefit achieved with VEGF-C and APMV
386 alone in an intervention treatment setting. Furthermore, we demonstrate long-term survival without tumor
387 recurrence beyond two years, whereas previous studies had endpoints at 50-100 days(*34, 35, 44*).
388 Notably, even after this extended period of observation, no metastases were detected. This finding is
389 particularly significant given the well-established role of tumor-derived VEGF-C in promoting metastatic
390 spread(*45, 46*). Our results underscore the fundamentally different outcome of VEGF-C expression in
391 the context of immune activation, where it orchestrates immune response and contributes to durable
392 tumor control and suppression of metastases.

393 The combination of VEGF-C and APMV reprograms the tumor immune microenvironment in multiple
394 ways to achieve tumor regression and we identified several hallmark changes associated with complete
395 response: (1) increased infiltration of $CD8^+$ and $CD4^+$ T cells; (2) activation of T cells and NK cells; (3)
396 expansion of specific effector and memory T cell subsets; and (4) reduction of inhibitory $CD4^+$ T cells and
397 immunosuppressive cues.

398 In the immunologically cold B16F10 melanoma model, VEGF-C expression induced lymphangiogenesis
399 and markedly increased intratumoral densities of $CD8^+$ and $CD4^+$ T cells. This is consistent with previous
400 studies linking lymphatic expansion to T cell accumulation(*34, 47*). T cell infiltration is a well-established
401 predictor of patient survival and response to immunotherapy across multiple cancer types(*48-52*). In our
402 study increased T cell presence alone was not sufficient to elicit anti-tumor responses, but it was a
403 prerequisite for mounting effective anti-tumor immunity upon APMV treatment. Consistent with this,
404 VEGF-C-expressing tumors harbored few $CD8^+$ and $CD4^+$ effector T cells, a low $CD8^+$ effector-to-Treg
405 ratio, and a high proportion of CXCR3+TIM3+ early exhausted $CD8^+$ T cells. These findings align with
406 prior reports indicating that VEGF-C alone does not impair tumor growth but may contribute to the
407 establishment of a tolerogenic tumor microenvironment(*53*).

408

409 APMV treatment of tumors in which TME has been altered with VEGF-C, shifts the tumor immune
410 landscape toward effector T cell phenotypes. Some of these changes were driven independently by
411 VEGF-C or APMV, and their combination likely produced additive effects, while some emerged only with
412 the VEGF-C/APMV combination, indicating synergy. One such synergistic effect was the unique
413 expansion of $CD8^+CD44^+PD\text{-}1^+CD25^+$ T cells correlated with CR. These cells represent recently
414 activated T cells in our model, since they were detected only 2.5 days after treatment initiation.

415 Prior studies have shown that PD-1 upregulation is a hallmark of early antigen-specific T cell activation
416 (*54*) and that the expression of co-inhibitory receptors alone does not indicate dysfunctional T cell
417 phenotype in melanoma (*55, 56*). $CD25^+PD\text{-}1^+CD8^+$ T cells have been identified as a key mediators of
418 effective antitumor immunity (*57, 58*) and they serve as a marker of effective T cell activation following
419 DC vaccination in melanoma (*59, 60*). In our study, robust expansion of $CD25^+PD\text{-}1^+$ effector $CD8^+$ T
420 cells and reduction of Tregs in NDV-treated B16/VEGF-C tumors, led to increased ratio of $CD25^+PD\text{-}$
421 1^+CD8^+ T cells to Tregs that was indicative of CR.

422 The mechanisms by which VEGF-C and APMV drive the expansion of $CD8^+CD25^+PD\text{-}1^+$ T cells remain
423 to be elucidated. VEGF-C-mediated lymphangiogenesis may create a supportive niche for proliferation
424 or retention of intratumoral TCF-1+ stem-like CD8+ T cells, which serve as precursors to $CD8^+PD\text{-}1^+$
425 effector cells and are essential for sustaining effector responses (*61*). Notably, both $TCF\text{-}1^+$ and memory
426 T cells have been shown to egress to sentinel LNs via lymphatics and are continuously replenished in
427 tumors by newly recruited cells (*62, 63*). Thus, expansion of lymphatic vasculature may facilitate
428 recirculation of T cells, thereby limiting exhaustion and supporting the maintenance of functional effector
429 populations.

430 Furthermore, APMV in combination with VEGF-C rapidly activates multiple effector cell populations,
431 including NK cells, $CD8^+$ and $CD4^+$ T cells. APMV alone strongly activated NK cells and induced GzmB+,
432 in agreement with prior studies (*6*). However, in the presence of VEGF-C, APMV increased GzmB+ CD8+
433 T cells, polyfunctional CD8 T cells and CD4+ effector T cells, while reducing exhausted-like TIM-3+ CD8+

434 subsets (*55, 64*), thus further increasing overall cytotoxic potential. While VEGF-C alone expanded
435 several effector-like $CD8^+$ subsets, APMV was necessary to trigger cytokine and GzmB production,
436 emphasizing that VEGF-C creates a receptive immune landscape, but APMV is required to trigger
437 effector engagement. The unique efficacy of APMV and VEGF-C combination likely reflects synergy of
438 NK and T cell responses, where APMV alone potently stimulates NK cells, and in combination with VEGF-
439 C also potently enhances T cell activation. Unlike checkpoint blockade, which primarily targets adaptive
440 immunity, this approach potently engages both innate and adaptive arms of the immune system.

441 In addition to promoting effector responses, VEGF-C/APMV treatment reduced immunosuppressive
442 $CD4^+$ T cell subsets expressing CD25 and CTLA-4, likely antigen-experienced cells which consume IL-2
443 and dampen $CD8^+$ T cell responses. Their diminished presence may contribute to reduced suppression,
444 enabling sustained $CD8^+$ T cell cytotoxicity. It has been suggested that one reason that NDV as a single
445 agent may not be sufficient to drive complete tumor rejection is because of inhibitory mechanisms induced
446 in response to the virus subsequent to activation (*40*). In line with this concept, we show that while NDV
447 initiated effector activation, it also increased suppressive $CD4^+$ T cells that may limit durable responses.
448 VEGF-C countered this feedback inhibition by reducing frequencies of $CD4^+$CTLA-4^+ Tregs, thus
449 enabling sustained co-stimulation and cytokine support. Hence, VEGF-C reduces inhibitory signals and
450 effectively abolishes CTLA-4-mediated suppression.

451 We demonstrate here that VEGF-C mRNA expression is a common feature across many solid tumors**.**
452 Our findings suggest that high VEGF-C expression may sensitize tumors to APMV-based virotherapy,
453 potentially identifying a subset of patients most likely to benefit clinically. For tumors with low
454 endogenous VEGF-C expression, exogenous delivery of VEGF-C may enhance therapeutic efficacy of
455 OVs. In melanoma, our data suggest that patients with high VEGF-C expression may be more likely to
456 respond favorably. In support of this idea, a clinical trial has shown that melanoma patients with
457 elevated serum VEGF-C levels experienced increased progression-free survival following checkpoint

458 inhibitor therapy (*34*). Further studies are needed to determine whether VEGF-C could help predict
459 therapeutic responses to APMVs and other oncolytic viruses.

460 In conclusion, in presence of VEGF-C, APMVs achieve complete response through multipronged
461 mechanisms; by increasing immune cell infiltration in tumors and by enhancing, accelerating and
462 sustaining immune activation. Our findings mark a significant advance by demonstrating the curative
463 potential of APMVs when VEGF-C is expressed in tumors. This lymphatic-focused approach represents
464 a promising novel strategy for enhancing efficacy of immunotherapies without overlapping toxicities,
465 particularly in tumors where checkpoint blockade has had limited impact.

466

467 **MATERIALS AND METHODS**

468 **Cells and culture conditions**

469 B16F10 cells were culture in DMEM (Gibco, cat. 11960-044) supplement with 10% FBS (Corning 35-
470 010-CV), L-glutamine 200mM (Gibco, cat. 25030-81) and Antibiotic-Antimycotic solution (Gibco, cat.
471 15240-062). Vero african green monkey kidney epithelial cells (ATCC Cat# CCL-81) were maintained in
472 DMEM medium supplemented with 10% FBS, 1% Glutamax-100X (Invitrogen), penicillin and
473 streptomycin (*1*). We received B16F10 – VEGF-C cells from Dr. Melody Swartz, (The University of
474 Chicago, Illinois, USA). To generate B16F10 empty vector (EV) cells we produced lentiviruses using
475 $CaCl_2$ transfection protocol. These lentiviruses carried a mammalian-expression empty vector (pD2109,
476 ATUMbio) (*35*). Briefly, viral envelope-encoding plasmids (pMD.2 and psPAX2) were mixed with empty
477 vector (EV) plasmid in a $CaCl_2$-HBSS 2X solution. Transfection particles were allowed to form for 30
478 minutes at room temperature and 1 ml of the solution was applied drop wise to an 80% confluent 293t
479 10 cm dish. 24 hours after transfection the conditioned media containing viruses was collected,
480 centrifuged at 1200 rpm for 5 minutes and filter through a 45 µm filter, aliquoted and stored at -80°C.
481 Then, $2x10^5$ B16F10 cells were seeded in a 60 mm dish supplemented with culture media. When cells
482 reached 50% confluency were transduced with 1 ml of the previously described lentivirus containing

483 media plus 1 ml of culture media. After 48 hours the media was replaced, and cells were grown for
484 another 72 hours to allow cells to express the desired transgene and the puromycin resistance gene.
485 When cells were confluent, they were transferred to a 10 cm dish. After 72h, media was replaced with
486 selection media containing 2 µg/ml puromycin (Sigma, cat. 540411). Cells were then culture in selection
487 media for 2 weeks.
488
489 **Avian Paramyxoviruses**
490 Modified NDV virus LaSota-L289A has been previously described (*65*). APMV-4 Duck/Hong
491 Kong/D3/1975 infectious clone used in these studies was previously reported (*36*). Viral stocks were
492 propagated in 9-day-old embryonated chicken eggs and clear purified from the allantoic fluid by
493 discontinuous sucrose density gradient ultracentrifugation for resuspension and storage in PBS. Viral
494 titers were calculated by indirect immunofluorescence on Vero cells using serotype-specific antiserums
495 to NDV (Rabbit polyclonal(*66*)) and to APMV-4 (475-ADV chicken polyclonal antiserum; USDA/NVSL).
496 Secondary antibodies, goat anti-rabbit Alexa Fluor 488 (A-11008) and anti-chicken Alexa Fluor 488 (A-
497 11039) were purchased from Invitrogen.
498
499 **Western Blot**
500 An 80% confluent 10 cm dish culture media was replaced with 1% FBS serum media for each cell line to
501 be analyzed for 12h. After 12h, media was collected, centrifuged at 1200 rpm for 5 minutes at 4°C, filtered
502 through a 40 µm filter (Fisher Scientific, cat. 22-363-547), aliquoted and stored at -80°C. 8 ml of the media
503 were then concentrated using Amicon 3K columns for protein concentration (Sigma Millipore cat.
504 UFC900324) for 1h at 4°C at 4000g. The collected supernatant was equalized to 300 µl with serum free
505 media. 15 µl of the concentrated media were supplemented with 5 µl of 6x Laemmli buffer, boiled at 96°C
506 for 5 minutes and loaded in a 15% acrylamide SDS-PAGE gel. The resolved gel was transferred to a
507 PVDF membrane (Biorad, cat. 1620177). Primary anti-VEGFC antibody (R&D, AF752) was diluted 1/100
508 in 5% milk-PBS-Tween 20 0.2% and incubated RT for 1h. Secondary anti-goat HRP (Jackson

509 Immunoresearch, Inc., Cat. 705-036-147) antibody was diluted 1:200 in 5% milk-PBS-Tween 20 0.2%
510 and incubated RT for 1h.
511
512 **RNA Isolation and qPCR**
513 RNA was extracted using QIAGEN RNeasy mini KIT (QIAGEN, cat.74104) according to manufacturer
514 instructions from a 90 – 100% confluent 10 cm dish of each cell line. 1 µg of RNA was used to produce
515 cDNA using iScript™ cDNA Synthesis Kit (Biorad, cat. 1708890) according to manufacturer instructions.
516 Resulting cDNA was diluted 1/10 and 2 µl of the dilution were used per reaction. qPCR was run in a 96
517 well plate using PowerUp™ SYBR™ Green Master Mix (Applied Biosystems, A25741) according to
518 manufacturer instructions in a OneStep qPCR machine (Applied Biosystems). Transcript expression was
519 normalized to the Actin and GADPH house-keeping gene and mRNA[RU] was calculated using the $2^{-\Delta\Delta CT}$
520 method for qPCR analysis. Primer sequences are described in the detailed methods (Extended Methods
521 Table 4).
522
523 **ELISA**
524 An 80% confluent 10 cm dish culture media was replaced with 1% FBS serum media for each cell line to
525 be analyzed for 12h. After 12h, media was collected, centrifuged at 1200 rpm for 5 minutes at 4°C, filtered
526 through a 45 µm filter, aliquoted and stored at -80°C. 100 µl of the conditioned media were used according
527 to manufacturer instructions (R&D, cat. DVEC00) to measure VEGF-C expression through ELISA. When
528 the conditioned media was collected cells were counted for normalization.
529
530 **Mouse experiments and tissue collection**
531 B16F10-EV or B16F10-VEGF-C tumor cells (3 x 10^5 cells in 100 µl serum-free media) were injected
532 intradermally into the right flank of seven to ten-week-old C57Bl/6J mice (Jackson, cat.000664). Mouse
533 weights and tumor sizes were measured every two days. Treatment was started when tumors reached 5
534 mm in size. 50 µL of a solution containing PBS, NDV or APMV-4 (10^7 PFUs/dose in 50 µL) were

535 administered to the mice intratumorally every two days for a total of 4 treatments. Mice were monitored
536 until humane endpoint. Mouse experiments were performed in accordance with protocols approved by
537 the Institutional Animal Care and Use Committee (IACUC). The formula $4/3\pi(\text{length}/2)^2(\text{width}/2)$ was
538 used to calculate tumor volume.
539
540 **Immunofluorescent staining and quantification**
541 For cell culture immunofluorescence, a well of a glass slide (ICN Biomedical, Cat.6041805) was seeded
542 with $5x10^4$ cells. After 12h, cells were washed with PBS and fixed in 10% formalin for 10 minutes RT.
543 Fixed cells were blocked with 1% goat serum in PBS-Tween 20 0.2% for 1h RT. Cells were then
544 incubated with anti-VEGFC primary antibody (R&D, cat. AF752) diluted 1/100 in 1% goat serum-PBS-
545 Tween 20 0.2% and incubated RT for 1h. Secondary anti-goat Alexa-594 antibody (Jackson
546 Immunoresearch, Inc, cat. 705-586-147) was diluted 1:500 in 1% goat serum PBS-Tween 20 0.2% and
547 incubated RT for 1h. Nuclei were counterstained with DAPI (1 µg/ml). Slides were coverslipped using
548 fluorescence mounting medium (Dako cat. S3023). Images were captured using the Nikon Eclipse E600
549 microscope and DS-Qi1 monochrome camera. For tissue immunofluorescence, fresh mouse tissues
550 were embedded in OCT (ThermoFisher, cat. 23-730-571) and sectioned at 6-7 µm on Cryostat (Leica
551 Biosystems, CM3050S). Sections were either stained immediately or stored at -80°C. Sections were fixed
552 in acetone on ice for 2 minutes, followed by 80% methanol for 5 minutes. Sections were washed with
553 PBS (Dulbecco's, no Ca or Mg, Gibco, cat. 14-190-250) 3 times for 5 minutes. Sections were then
554 incubated in primary antibody (Extended Methods Table 2) in antibody diluent (PBS, 12% BSA, 0.01%
555 NaN3) in a humidified chamber. Sections were washed 3 times for 5 minutes in PBS and then incubated
556 in the corresponding fluorescent conjugated secondary antibody for 1 hour at room temperature in a dark
557 humidified chamber. Sections were washed again 3 times for 5 minutes in PBS and incubated in DAPI 1
558 µg/mL for 30 seconds. Sections were washed 3 times for 5 minutes in PBS and coverslipped using DAKO
559 Fluorescent Mounting Media (Agilent, S3023).
560

561 **Immunohistochemistry**

562 Immunohistochemistry was performed on paraffin-embedded tissue sections using the Leica Bond RX
563 automated Immunostainer (Leica Biosystems), according to the Leica staining protocol. Briefly, all slides
564 were deparaffinized using a heated Bond™ Dewax Solution (Leica cat. AR9222) and washed with 1X
565 Bond™ Wash Solution (Leica cat. AR9590). Epitope retrievals were carried out for 20 minutes using the
566 citrate-based Bond™ Epitope Retrieval 1 solution (Leica cat. AR9961) or solution 2 (Leica cat. AR9961).
567 Slides were then blocked with either the Dako Dual Endogenous Enzyme Block (Agilent, S2003) for ten
568 minutes prior to staining with the Bond™ Polymer Refine Red Detection System (Leica cat. DS9390), or
569 with a 3-4% v/v hydrogen peroxide block for five minutes that is incorporated into the Bond™ Polymer
570 Refine Detection kit (Leica cat. DS9800) and used for DAB staining. Melan A antibody was diluted in
571 Bond™ Primary Antibody Diluent (Leica Biosystems, AR9352). Slides were mounted Glycergel Aqueous
572 Mounting Media (DAKO, cat. C0563) or Cytoseal XYL (Fisher Scientific, cat.50-209-0573). A list of
573 antibodies and experimental conditions can be found in Extended Methods Table 3 and 4.

574

575 **Spectral Flow Cytometry**

576 Spectral Flow cytometry was performed using Aurora Spectral Cytometer (Cytek Biosciences) or and
577 flow cytometry using LSR Fortessa X-20 (BD Biosciences). In brief, tissues were dissected and minced
578 in a sterile petri dish in ice cold PBS. Tumor tissues were dissociated with Mouse Tumor Dissociation Kit
579 (Miltenyi, cat. 130-096-730) enzymes in Octomacs Dissociator with Heaters (Miltenyi, cat. 130-096-427).
580 Lymph nodes were dissociated with Collagenase D enzyme (1 mg/ml, Roche, cat. 50-100-3282) in 37°C
581 water bath for 1h. Dissociation reactions were stopped with the addition of ice-cold FACS buffer (1%FBS,
582 0.09% NaN3 in PBS). Erythrocytes were lysed using RBC lysis (cat. 00-4300-54, eBioscience) for 1
583 minute on ice. Lysis was stopped by the addition of ice-cold FACS buffer. Dissociated tissues were
584 pressed through a 70 µm nylon filter (Fisher Scientific, cat. 22-363-548) to create a single cell suspension.
585 Cell yield and viability were determined using Countess II Automated Cell Counter (ThermoFisher).
586 Samples were stained with primary antibodies (Extended Methods Table 1) targeting cell surface markers

587 for 30 minutes on ice (10^6 cells/100 µL). They were then fixed and permeabilized with FOXP3
588 Transcription Factor Staining Buffer Set (cat. 00-5523-00, eBioscience). Samples were then stained with
589 primary antibodies targeting intracellular markers. Compensation and reference groups were calculated
590 using UltraComp beads (cat. 01-2222-41, eBioscience). Dead cells were excluded using LIVE/DEAD
591 Fixable Yellow Dead Cell Stain Kit (cat. L34968, Invitrogen). $2.0x10^4$-$1.0x10^5$ viable $CD45^+$ cells were
592 acquired/sample. Flow cytometry data analysis was performed on FCS Express Version 7.0.
593
594 **Image processing and analysis**
595 Slides were scanned with Nanazoomer Digital Slide Scanner (Hamamtsu, Shizuoka, Japan). Image
596 processing was performed using NDP viewer 2 (Hamamatsu, Shizuoka, Japan) and analyzed using Fiji
597 open-source software v.1.53q (National Institutes of Health). Confocal images were acquired at the
598 Microscopy and Advanced Bioimaging CoRE at the Icahn School of Medicine at Mount Sinai using a
599 ZEISS LSM 780 Laser Scanning Microscope (ZEISS, USA). Image processing and analysis was
600 performed using Fiji open-source softwarev.1.53q (National Institutes of Health). For quantification of
601 cells, single channel 8-bit scanned images of complete tumor sections were analyzed using count
602 particles Fiji tool. 3 to 5 different whole tumor sections were counted per experimental group. T cell
603 distance to LYVE-1^+ cells was performed using Qupath (v 0.5.1). Regions of interest were drawn for each
604 tumor we done using the polygon annotation tool. Next, cell detections were performed within each region
605 of interest using DAPI (blue) channel to detect the nucleus of individual cells. LYVE-1 (green) and CD8
606 or CD4 (red) channels were used to detect and quantify LYVE-1^+, $CD8^+$ and $CD4^+$ cells, respectively.
607 Spatial analysis was performed to detect centroid distances in 2D and distance annotations in 2D.
608
609 **Aurora spectral flow cytometry data analysis**
610 High-dimensional flow cytometry data was clustered using Clustergrammer web-based tool (*67*). To
611 ensure that each treatment group is represented by the same number of cells, we randomly subsampled
612 cells from mice subjected to the same treatment. The number of subsampled cells per treatment was

613 equal to the lowest number of cells over all treatments. The proportions of cells subsampled from each
614 mouse were held constant to reflect the original proportions over all mice belonging to one treatment.
615 Using the subsampled data set we tested whether there is a significant difference in the distribution of
616 cells coming from different treatments using the Chi-square test for overall difference in the distribution
617 of phenotypes across treatments and for pairwise comparisons of all combinations of different treatments.
618 P-values were corrected for multiple testing using the Bonferroni correction. Effect size of the Chi-square
619 test was evaluated by Cohen's W (reference) for overall and pairwise differences in distribution Cohen's
620 W was calculated using the implementation in the Rcompanion package for R statistical environment
621 (Mangiafico, 2022). We considered Cohen's W larger or equal to 0.5 to represent a large effect size, 0.30
622 – 0.50 medium effect size, 0.1 – 0.3 small effect and less than 0.1 no effect. We removed all the
623 phenotypes where the cell type could not be precisely determined and for the remaining phenotypes, we
624 calculated the median of marker expression values (signal intensity) for clusters of cells belonging to
625 each phenotype. 9 populations in the non-draining lymph node with the same markers and same
626 distribution were condensed into 4 different populations to form B cells 2, $CD8^+$ T cells 2, $CD8^+$ T cells
627 14, and $CD8^+$ T cells 15. The observed proportion, relative effect size and p-value of these population
628 was not significantly altered after the merge.
629
630 **TCGA analysis**
631 TCGA Pan-Cancer Atlas (PANCAN) 2022 transcriptomic data sets (bulk RNA-seq) were analyzed using
632 hegemon web-based tool (http://hegemon.ucsd.edu/Tools/). VEGF-C mRNA expression was analyzed
633 across 31 solid tumor types, comprising a total of 10,839 tumor samples. Tumors were classified as
634 having high or low VEGF-C expression based on the median log_2(TPMK) value across all tumors from
635 different cancer types.
636
637 **Statistical analyses**

Statistical analyses were performed using GraphPad Prism (v.10) software and each specific statistical test is indicated in the corresponding figure legend.

List of Supplementary Materials:

Supplementary Materials and Methods

Supplementary Figures S1 to S9

Data files

Extended methods tables

ACKNOWLEDGEMENTS

We would like to thank the expertise and assistance of the Dean's Flow Cytometry CORE and the Microscopy and Advanced Bioimaging CoRE at the Icahn School of Medicine at Mount Sinai. This research was supported in part by the Tisch Cancer Institute at Mount Sinai P30 CA196521 – Cancer Center Support Grant.

Funding: This research was supported by the grant from Pershing Square Philantropies (M.S.).

Author contributions:

Conceptualization: RFR, SCC, AGS, MS

Methodology: RFR, SCC, AE, AR, NDF, IM, RK, AH

Investigation: RFR, SCC, AE, AR, YB, RK, IM, AK, AH

Visualization: RFR, RK

Funding acquisition: AGS, MS

Project administration: RFR, SCC, AGS, MS

Supervision: MS, AGS

Writing – original draft: RFR, MS

Writing – review & editing: RFR, SCC, YB, AK, AH, AGS, MS

Conflict of Interests: A.G.S. has received research support from Pfizer, Senhwa Biosciences, Kenall Manufacturing, Avimex, Johnson & Johnson, Dynavax, 7Hills Pharma, Pharmamar, ImmunityBio, Accurius Therapeutics Inc., Nanocomposix, Hexamer, N-fold LLC, Model Medicines, Atea Pharma and Merck. A.G.S. has consulting agreements for the following companies involving cash and/or stock: Vivaldi Biosciences, Contrafect, 7Hills Pharma, Pagoda, Accurius, Esperovax, Farmak, Applied Biological Laboratories, Pharmamar, Paratus, CureLab Oncology, CureLab Veterinary, Amovir, Virofend and Pfizer. S.C.C is co-founder and CSO of ViroFend Therapeutics S.L. A.G.S. is scientific advisor and board member at ViroFend Therapeutics S. L. S.C.C and A.G.S. are inventors in patents associated with the use of viruses as cancer therapeutics.

R.F.R., S.C.C., A.K.E., I.M., A.G.S. and M.S report a patent for use of APMV in combination with VEGFR-3 activating molecules.

Alice Kamphorst does not report any conflict of interest.

Amir Horowitz does not report any conflict of interest.

Rosa Karlic does not report any conflict of interest.

Noelia Dasilva-Freire does not report any conflict of interest.

Yonina Bikov does not report any conflict of interest.

691 **REFERENCES**

692

693 1. Y. Bykov, G. Dawodu, A. Javaheri, A. Garcia-Sastre, S. Cuadrado-Castano, Immune responses
694 elicited by ssRNA(-) oncolytic viruses in the host and in the tumor microenvironment. *Journal of*
695 *Cancer Metastasis and Treatment*, (2023).
696 2. K. J. Hiam-Galvez, B. M. Allen, M. H. Spitzer, Systemic immunity in cancer. *Nature Reviews*
697 *Cancer* **21**, 345-359 (2021).
698 3. S. Z. Shalhout, D. M. Miller, K. S. Emerick, H. L. Kaufman, Therapy with oncolytic viruses:
699 progress and challenges. *Nature Reviews Clinical Oncology* **20**, 160-177 (2023).
700 4. G. Vijayakumar, P. Palese, P. H. Goff, Oncolytic Newcastle disease virus expressing a
701 checkpoint inhibitor as a radioenhancing agent for murine melanoma. *EBioMedicine* **49**, 96-105
702 (2019).
703 5. G. Vijayakumar, D. Zamarin, Design and Production of Newcastle Disease Virus for Intratumoral
704 Immunomodulation. *Methods Mol Biol* **2058**, 133-154 (2020).
705 6. B. Burman, G. Pesci, D. Zamarin, Newcastle Disease Virus at the Forefront of Cancer
706 Immunotherapy. *Cancers* **12**, 3552 (2020).
707 7. D. Davar *et al.*, Phase I study of a recombinant attenuated oncolytic virus, MEDI5395 (NDV–
708 GM-CSF), administered systemically in combination with durvalumab in patients with advanced
709 solid tumors. *Journal for ImmunoTherapy of Cancer* **12**, e009336 (2024).
710 8. P. K. Bommareddy, A. Patel, S. Hossain, H. L. Kaufman, Talimogene Laherparepvec (T-VEC)
711 and Other Oncolytic Viruses for the Treatment of Melanoma. *Am J Clin Dermatol* **18**, 1-15
712 (2017).
713 9. H. L. Kaufman, S. Z. Shalhout, G. Iodice, Talimogene Laherparepvec: Moving From First-In-
714 Class to Best-In-Class. *Frontiers in Molecular Biosciences* **9**, (2022).
715 10. P. Muthukutty, S. Y. Yoo, Oncolytic Virus Engineering and Utilizations: Cancer Immunotherapy
716 Perspective. *Viruses*. 2023 (10.3390/v15081645).
717 11. N. I. Khushalani, K. J. Harrington, A. Melcher, P. K. Bommareddy, D. Zamarin, Breaking the
718 barriers in cancer care: The next generation of herpes simplex virus-based oncolytic
719 immunotherapies for cancer treatment. *Mol Ther Oncolytics* **31**, 100729 (2023).
720 12. R. A. Lamb, & Parks, G. D., *Paramyxoviridae: the viruses and their replication*. D. M. K. B. N.
721 Fields, & P. M. Howley Ed., (Lippincott, Williams, and Wilkins, Philadelphia, ed. 6th, 2013), vol.
722 1.
723 13. D. Zamarin *et al.*, Enhancement of oncolytic properties of recombinant newcastle disease virus
724 through antagonism of cellular innate immune responses. *Mol Ther* **17**, 697-706 (2009).

725 14. D. Zamarin, P. Palese, Oncolytic Newcastle disease virus for cancer therapy: old challenges
726 and new directions. *Future Microbiol* **7**, 347-367 (2012).
727 15. D. Zamarin *et al.*, Localized oncolytic virotherapy overcomes systemic tumor resistance to
728 immune checkpoint blockade immunotherapy. *Sci Transl Med* **6**, 226ra232 (2014).
729 16. V. Schirrmacher, Fifty Years of Clinical Application of Newcastle Disease Virus: Time to
730 Celebrate! *Biomedicines* **4**, (2016).
731 17. D. Zamarin *et al.*, Intratumoral modulation of the inducible co-stimulator ICOS by recombinant
732 oncolytic virus promotes systemic anti-tumour immunity. *Nat Commun* **8**, 14340 (2017).
733 18. D. Zamarin, J. D. Wolchok, Potentiation of immunomodulatory antibody therapy with oncolytic
734 viruses for treatment of cancer. *Mol Ther Oncolytics* **1**, 14004 (2014).
735 19. P. Li *et al.*, Therapeutic effects of a fusogenic newcastle disease virus in treating head and neck
736 cancer. *Head Neck* **33**, 1394-1399 (2011).
737 20. S. Cuadrado-Castano *et al.*, Enhancement of the proapoptotic properties of newcastle disease
738 virus promotes tumor remission in syngeneic murine cancer models. *Mol Cancer Ther* **14**, 1247-
739 1258 (2015).
740 21. G. Vijayakumar, S. McCroskery, P. Palese, Engineering Newcastle Disease Virus as an
741 Oncolytic Vector for Intratumoral Delivery of Immune Checkpoint Inhibitors and
742 Immunocytokines. *J Virol* **94**, (2020).
743 22. J. Elmberg, C. Berg, H. Lerner, J. Waldenstrom, R. Hessel, Potential disease transmission from
744 wild geese and swans to livestock, poultry and humans: a review of the scientific literature from
745 a One Health perspective. *Infect Ecol Epidemiol* **7**, 1300450 (2017).
746 23. K. Maisel, M. S. Sasso, L. Potin, M. A. Swartz, Exploiting lymphatic vessels for
747 immunomodulation: Rationale, opportunities, and challenges. *Advanced Drug Delivery Reviews*
748 **114**, 43-59 (2017).
749 24. B. A. J. Tamburini, T. P. Padera, A. W. Lund, Editorial: Regulation of Immune Function by the
750 Lymphatic Vasculature. *Front Immunol* **10**, 2597 (2019).
751 25. L. Garnier, A. O. Gkountidi, S. Hugues, Tumor-Associated Lymphatic Vessel Features and
752 Immunomodulatory Functions. *Front Immunol* **10**, 720 (2019).
753 26. T. Karakousi, T. Mudianto, A. W. Lund, Lymphatic vessels in the age of cancer immunotherapy.
754 *Nature Reviews Cancer*, (2024).
755 27. M. Jeltsch *et al.*, Hyperplasia of lymphatic vessels in VEGF-C transgenic mice. *Science* **276**,
756 1423-1425 (1997).
757 28. V. Joukov *et al.*, A novel vascular endothelial growth factor, VEGF-C, is a ligand for the Flt4
758 (VEGFR-3) and KDR (VEGFR-2) receptor tyrosine kinases. *EMBO J* **15**, 290-298 (1996).

759 29. V. Joukov *et al.*, Proteolytic processing regulates receptor specificity and activity of VEGF-C.
760 *EMBO J* **16**, 3898-3911 (1997).
761 30. M. Jeltsch *et al.*, CCBE1 Enhances Lymphangiogenesis via A Disintegrin and Metalloprotease
762 With Thrombospondin Motifs-3-Mediated Vascular Endothelial Growth Factor-C Activation.
763 *Circulation* **129**, 1962-1971 (2014).
764 31. L. Le Guen *et al.*, Ccbe1 regulates Vegfc-mediated induction of Vegfr3 signaling during
765 embryonic lymphangiogenesis. *Development* **141**, 1239-1249 (2014).
766 32. M. G. Roukens *et al.*, Functional Dissection of the CCBE1 Protein: A Crucial Requirement for
767 the Collagen Repeat Domain. *Circ Res* **116**, 1660-1669 (2015).
768 33. H. M. Bui *et al.*, Proteolytic activation defines distinct lymphangiogenic mechanisms for VEGFC
769 and VEGFD. *J Clin Invest* **126**, 2167-2180 (2016).
770 34. M. Fankhauser *et al.*, Tumor lymphangiogenesis promotes T cell infiltration and potentiates
771 immunotherapy in melanoma. *Sci Transl Med* **9**, (2017).
772 35. M. S. Sasso *et al.*, Lymphangiogenesis-inducing vaccines elicit potent and long-lasting T cell
773 immunity against melanomas. *Science Advances* **7**, eabe4362 (2021).
774 36. A. Javaheri, Y. Bykov, I. Mena, A. García-Sastre, S. Cuadrado-Castano, Avian Paramyxovirus 4
775 Antitumor Activity Leads to Complete Remissions and Long-term Protective Memory in
776 Preclinical Melanoma and Colon Carcinoma Models. *Cancer Research Communications* **2**, 602-
777 615 (2022).
778 37. A. Van Elsas, A. A. Hurwitz, J. P. Allison, Combination Immunotherapy of B16 Melanoma Using
779 Anti–Cytotoxic T Lymphocyte–Associated Antigen 4 (Ctla-4) and Granulocyte/Macrophage
780 Colony-Stimulating Factor (Gm-Csf)-Producing Vaccines Induces Rejection of Subcutaneous
781 and Metastatic Tumors Accompanied. *Journal of Experimental Medicine* **190**, 355-366 (1999).
782 38. H. Salmon *et al.*, Expansion and Activation of CD103(+) Dendritic Cell Progenitors at the Tumor
783 Site Enhances Tumor Responses to Therapeutic PD-L1 and BRAF Inhibition. *Immunity* **44**, 924-
784 938 (2016).
785 39. J. Svensson-Arvelund *et al.*, Expanding cross-presenting dendritic cells enhances oncolytic
786 virotherapy and is critical for long-term anti-tumor immunity. *Nat Commun* **13**, 7149 (2022).
787 40. D. Zamarin *et al.*, PD-L1 in tumor microenvironment mediates resistance to oncolytic
788 immunotherapy. *Journal of Clinical Investigation* **128**, 1413-1428 (2018).
789 41. J. Harper *et al.*, Recombinant Newcastle Disease Virus Immunotherapy Drives Oncolytic Effects
790 and Durable Systemic Antitumor Immunity. *Mol Cancer Ther* **20**, 1723-1734 (2021).
791 42. K. Harrington, D. J. Freeman, B. Kelly, J. Harper, J.-C. Soria, Optimizing oncolytic virotherapy in
792 cancer treatment. *Nature Reviews Drug Discovery* **18**, 689-706 (2019).

793 43. X. Xu *et al.*, Tumor Cells Modified with Newcastle Disease Virus Expressing IL-24 as a Cancer
794 Vaccine. *Molecular Therapy - Oncolytics* **14**, 213-221 (2019).
795 44. E. Song *et al.*, VEGF-C-driven lymphatic drainage enables immunosurveillance of brain
796 tumours. *Nature* **577**, 689-694 (2020).
797 45. M. Skobe *et al.*, Induction of tumor lymphangiogenesis by VEGF-C promotes breast cancer
798 metastasis. *Nat Med* **7**, 192-198 (2001).
799 46. M. Skobe, B. Pytowski, in *Tumor Angiogenesis: A Key Target for Cancer Therapy,* D. Marmé,
800 Ed. (Springer International Publishing, Cham, 2019), pp. 1-23.
801 47. N. Bordry *et al.*, Lymphatic vessel density is associated with CD8+ T cell infiltration and
802 immunosuppressive factors in human melanoma. *OncoImmunology* **7**, e1462878 (2018).
803 48. J. Galon *et al.*, Type, density, and location of immune cells within human colorectal tumors
804 predict clinical outcome. *Science* **313**, 1960-1964 (2006).
805 49. R. S. Herbst *et al.*, Predictive correlates of response to the anti-PD-L1 antibody MPDL3280A in
806 cancer patients. *Nature* **515**, 563-567 (2014).
807 50. Y. Naito *et al.*, CD8+ T cells infiltrated within cancer cell nests as a prognostic factor in human
808 colorectal cancer. *Cancer Res* **58**, 3491-3494 (1998).
809 51. P. C. Tumeh *et al.*, PD-1 blockade induces responses by inhibiting adaptive immune resistance.
810 *Nature* **515**, 568-571 (2014).
811 52. F. Azimi *et al.*, Tumor-infiltrating lymphocyte grade is an independent predictor of sentinel lymph
812 node status and survival in patients with cutaneous melanoma. *J Clin Oncol* **30**, 2678-2683
813 (2012).
814 53. A. W. Lund *et al.*, VEGF-C promotes immune tolerance in B16 melanomas and cross-
815 presentation of tumor antigen by lymph node lymphatics. *Cell Rep* **1**, 191-199 (2012).
816 54. S. J. Judge *et al.*, Minimal PD-1 expression in mouse and human NK cells under diverse
817 conditions. *Journal of Clinical Investigation* **130**, 3051-3068 (2020).
818 55. M. Singer *et al.*, A Distinct Gene Module for Dysfunction Uncoupled from Activation in Tumor-
819 Infiltrating T Cells. *Cell* **166**, 1500-1511 e1509 (2016).
820 56. I. Tirosh *et al.*, Dissecting the multicellular ecosystem of metastatic melanoma by single-cell
821 RNA-seq. *Science* **352**, 189-196 (2016).
822 57. D. Herndler-Brandstetter *et al.*, CD25-expressing CD8+ T cells are potent memory cells in old
823 age. *J Immunol* **175**, 1566-1574 (2005).
824 58. W. Wu *et al.*, IL-2Ralpha-biased agonist enhances antitumor immunity by invigorating tumor-
825 infiltrating CD25(+)CD8(+) T cells. *Nat Cancer* **4**, 1309-1325 (2023).

826 59. P. M. Santos *et al.*, Impact of checkpoint blockade on cancer vaccine-activated CD8+ T cell
827 responses. *J Exp Med* **217**, (2020).
828 60. M. Grees *et al.*, Optimized dendritic cell vaccination induces potent CD8 T cell responses and
829 anti-tumor effects in transgenic mouse melanoma models. *Oncoimmunology* **7**, e1445457
830 (2018).
831 61. I. Siddiqui *et al.*, Intratumoral Tcf1+PD-1+CD8+ T Cells with Stem-like Properties Promote
832 Tumor Control in Response to Vaccination and Checkpoint Blockade Immunotherapy. *Immunity*
833 **50**, 195-211.e110 (2019).
834 62. Z. Li *et al.*, In vivo labeling reveals continuous trafficking of TCF-1+ T cells between tumor and
835 lymphoid tissue. *Journal of Experimental Medicine* **219**, (2022).
836 63. K. A. Connolly *et al.*, A reservoir of stem-like CD8(+) T cells in the tumor-draining lymph node
837 preserves the ongoing antitumor immune response. *Sci Immunol* **6**, eabg7836 (2021).
838 64. S. Kurtulus *et al.*, Checkpoint Blockade Immunotherapy Induces Dynamic Changes in PD-1(-
839)CD8(+) Tumor-Infiltrating T Cells. *Immunity* **50**, 181-194 e186 (2019).
840 65. W. Liang *et al.*, Application of autologous tumor cell vaccine and NDV vaccine in treatment of
841 tumors of digestive tract. *World journal of gastroenterology : WJG* **9**, 495-498 (2003).
842 66. M. S. Park, A. Garcia-Sastre, J. F. Cros, C. F. Basler, P. Palese, Newcastle disease virus V
843 protein is a determinant of host range restriction. *J Virol* **77**, 9522-9532 (2003).
844 67. N. F. Fernandez *et al.*, Clustergrammer, a web-based heatmap visualization and analysis tool
845 for high-dimensional biological data. *Sci Data* **4**, 170151 (2017).
846

Figure 1

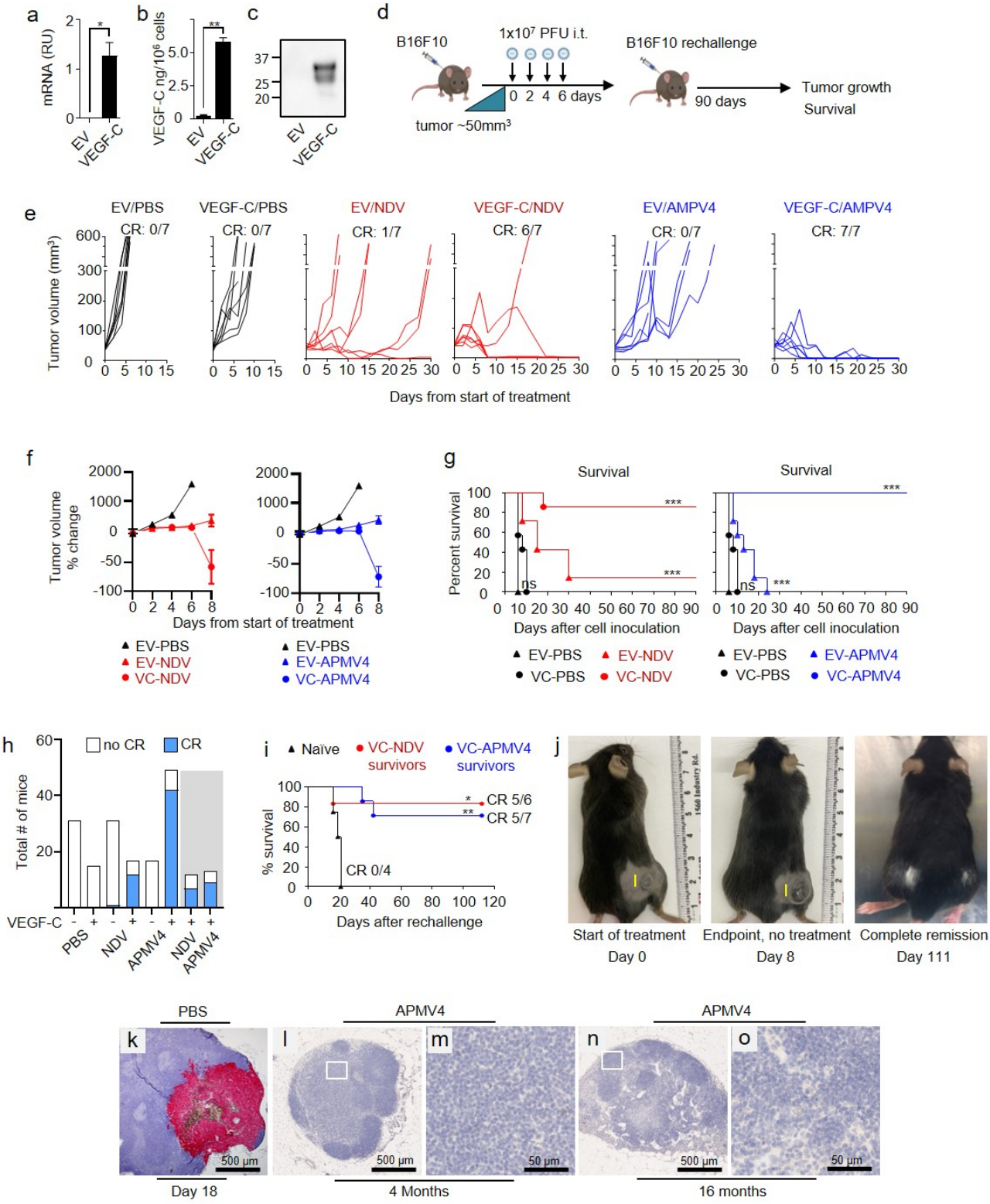
a
mRNA (RU)
EV
VEGF-C
b
VEGF-C ng/10⁶ cells
c
37
25
20
d
B16F10
1x10⁷ PFU i.t.
0 2 4 6 days
tumor ~50mm³
B16F10 rechallenge
90 days
Tumor growth
Survival
e
EV/PBS
CR: 0/7
VEGF-C/PBS
CR: 0/7
EV/NDV
CR: 1/7
VEGF-C/NDV
CR: 6/7
EV/AMPV4
CR: 0/7
VEGF-C/AMPV4
CR: 7/7
Tumor volume (mm³)
Days from start of treatment
f
Tumor volume % change
Days from start of treatment
EV-PBS
EV-NDV
VC-NDV
EV-PBS
EV-APMV4
VC-APMV4
g
Survival
Percent survival
Days after cell inoculation
EV-PBS
EV-NDV
VC-PBS
VC-NDV
EV-PBS
EV-APMV4
VC-PBS
VC-APMV4
h
no CR
CR
Total # of mice
VEGF-C
PBS
NDV
APMV4
NDV
APMV4
i
Naïve
VC-NDV survivors
VC-APMV4 survivors
% survival
CR 5/6
CR 5/7
CR 0/4
Days after rechallenge
j
Start of treatment
Day 0
Endpoint, no treatment
Day 8
Complete remission
Day 111
PBS
APMV4
APMV4
k
l
m
n
o
500 µm
500 µm
50 µm
500 µm
50 µm
Day 18
4 Months
16 months

Fig 1. VEGF-C enhances the anti-tumor efficacy of APMVs in the B16F10 tumor model. (a-c) VEGF-C expression by B16F10 melanoma cells, transduced with mVEGF-C or an empty vector (EV), determined by qPCR (a), ELISA (b), and Western blot (c). Error bars represent mean ± SEM, n=2. Statistics: unpaired t-test p=0.0417 (a) and p=0.029 (b). (d) Experimental design: Mice were injected with $3x10^5$ B16F10/EV or B16F10/VEGF-C cells. Treatment began when tumors reached ~$50mm^3$. NDV, APMV4 or PBS were administered intratumorally four times, every two days, and mice were monitored for tumor growth and survival. (e) B16/EV and B16/VEGF-C tumor growth upon treatments as indicated. Individual tumor growth curves are shown. (f) Tumor volume percentage change relative to the start of treatment over the first eight days. Error bars represent mean ± SEM, n=7 (g) Survival of mice bearing B16/EV or B16/VEGF-C tumors, treated with PBS, NDV, or APMV-4, as indicated. Statistical analysis: Log-rank (Mantel-Cox) test, n=7. (h) Cumulative data from all experiments showing total number of mice per experimental condition, number of mice in each group achieving complete remission (blue), and those not achieving complete remission (white). Gray shaded area indicates rechallenge experiments. (i) Survival of mice rechallenged with B16F10/EV cells 90 days after achieving complete remission (CR) following treatment of B16/VEGF-C tumors with NDV or APMV4. Statistical analysis: Log-rank (Mantel-Cox) test. (j) Representative images of mice at three time points: left, start of the treatment; center, humane end-point untreated mouse; right, mouse in complete remission after NDV treatment of B16F10/VEGF-C tumors and subsequent rechallenge. White patch of hair on the site of the first regressed tumor (right hind limb) and on the site of rechallenge (left hind limb). (k-o) Melan-A staining for detection of B16 melanoma metastases. Representative images of sentinel (inguinal) LNs of mice bearing B16F10/VEGF-C tumors, treated with PBS (n=18, 2 experiments) or APMV4 (n=23, 4 experiments) at indicated time-points after the start of treatment. In vivo experiments were independently conducted 2-8 times. *p<0.05 **p<0.01 ***p<0.001, ns = not significant. Scale bars: i, 5 mm; k, m, o, 500 μm; l, n, 50 μm.

Figure 2

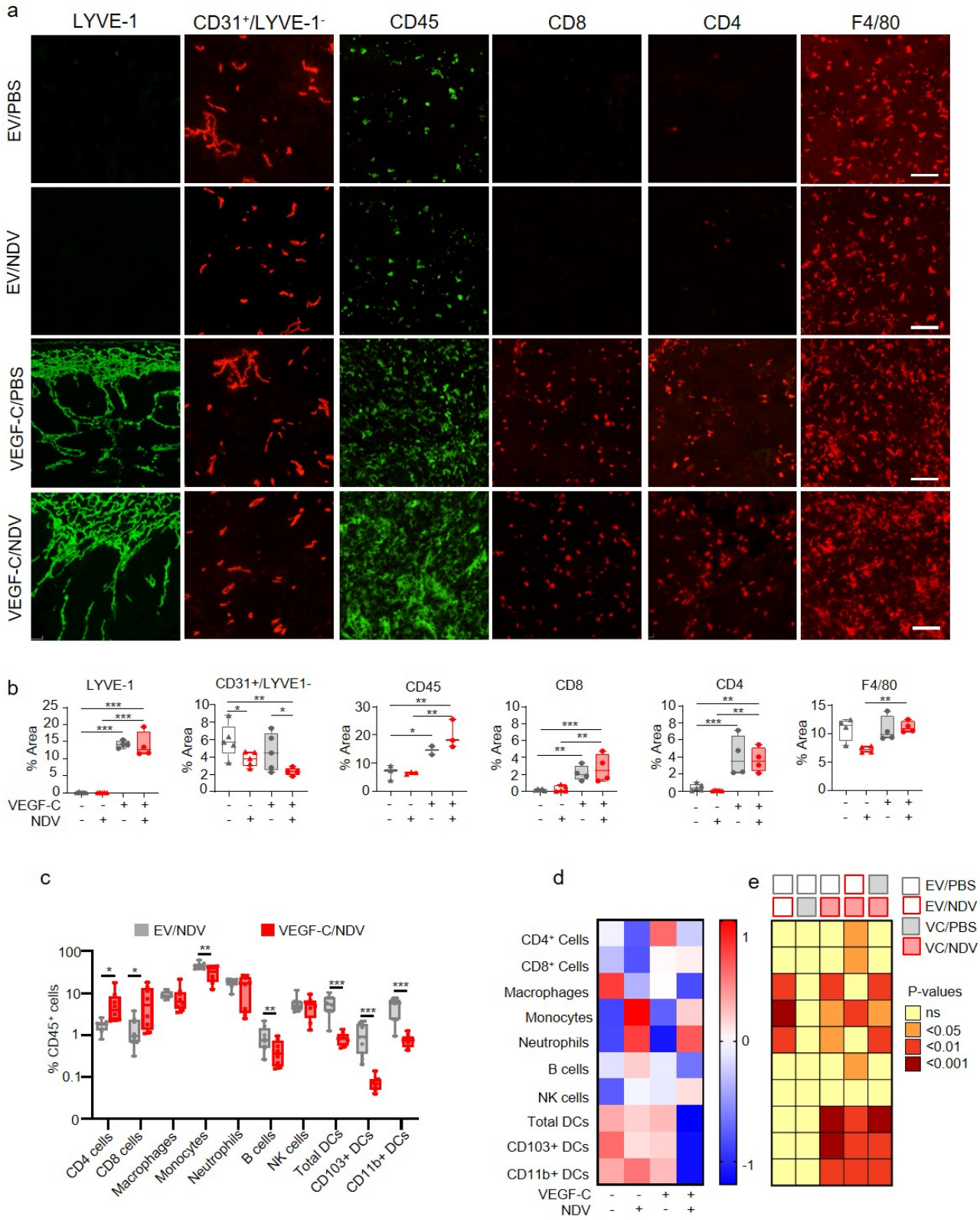
a
LYVE-1
CD31+/LYVE-1-
CD45
CD8
CD4
F4/80
EV/PBS
EV/NDV
VEGF-C/PBS
VEGF-C/NDV
b
LYVE-1
CD31+/LYVE1-
CD45
CD8
CD4
F4/80
% Area
VEGF-C
NDV
c
EV/NDV
VEGF-C/NDV
% CD45+ cells
CD4 cells
CD8 cells
Macrophages
Monocytes
Neutrophils
B cells
NK cells
Total DCs
CD103+ DCs
CD11b+ DCs
d
CD4+ Cells
CD8+ Cells
Macrophages
Monocytes
Neutrophils
B cells
NK cells
Total DCs
CD103+ DCs
CD11b+ DCs
VEGF-C
NDV
e
EV/PBS
EV/NDV
VC/PBS
VC/NDV
P-values
ns
<0.05
<0.01
<0.001

Fig 2. Effects of VEGF-C and NDV on tumor vasculature and immune cells. (a, b) Immunofluorescent staining (IF) of B16/EV and B16/VEGF-C tumors treated with PBS or NDV, for lymphatics (LYVE-1), blood vessels (CD31+/LYVE-1-), and immune cells, as indicated. Representative images (a), and quantification of immunostaining (b). Box-and-whiskers plots show individual values with mean ± SEM, and whiskers spanning the full range; EV/PBS, n=5; EV/NDV, n=5; VEGF-C/PBS, n=4; VEGF-C/NDV, n=4. (c) Immunophenotyping of NDV-treated B16/EV and B16/VEGF-C tumors by spectral flow cytometry. Frequencies of distinct myeloid and T cell subtypes as a percentage of total CD45 cells are shown. Box-and-whiskers plots show individual values with mean ± SEM, and whiskers spanning the full range; EV/NDV, n=8; VEGF-C/NDV, n=8. Outliers were removed based on ROUT analysis. Q=0.5%. (d) Heatmap displaying z-score values of various immune cell populations in B16 tumors, as indicated. (e) Heatmap displaying p-values for the multiple comparisons between the populations in (d). Statistical analysis with one-way ANOVA multiple comparisons Fisher LSD test. *$p < 0.05$, **$p < 0.01$, ***$p < 0.001$, ns = not significant. Scale bars: 100 μm.

Figure 3

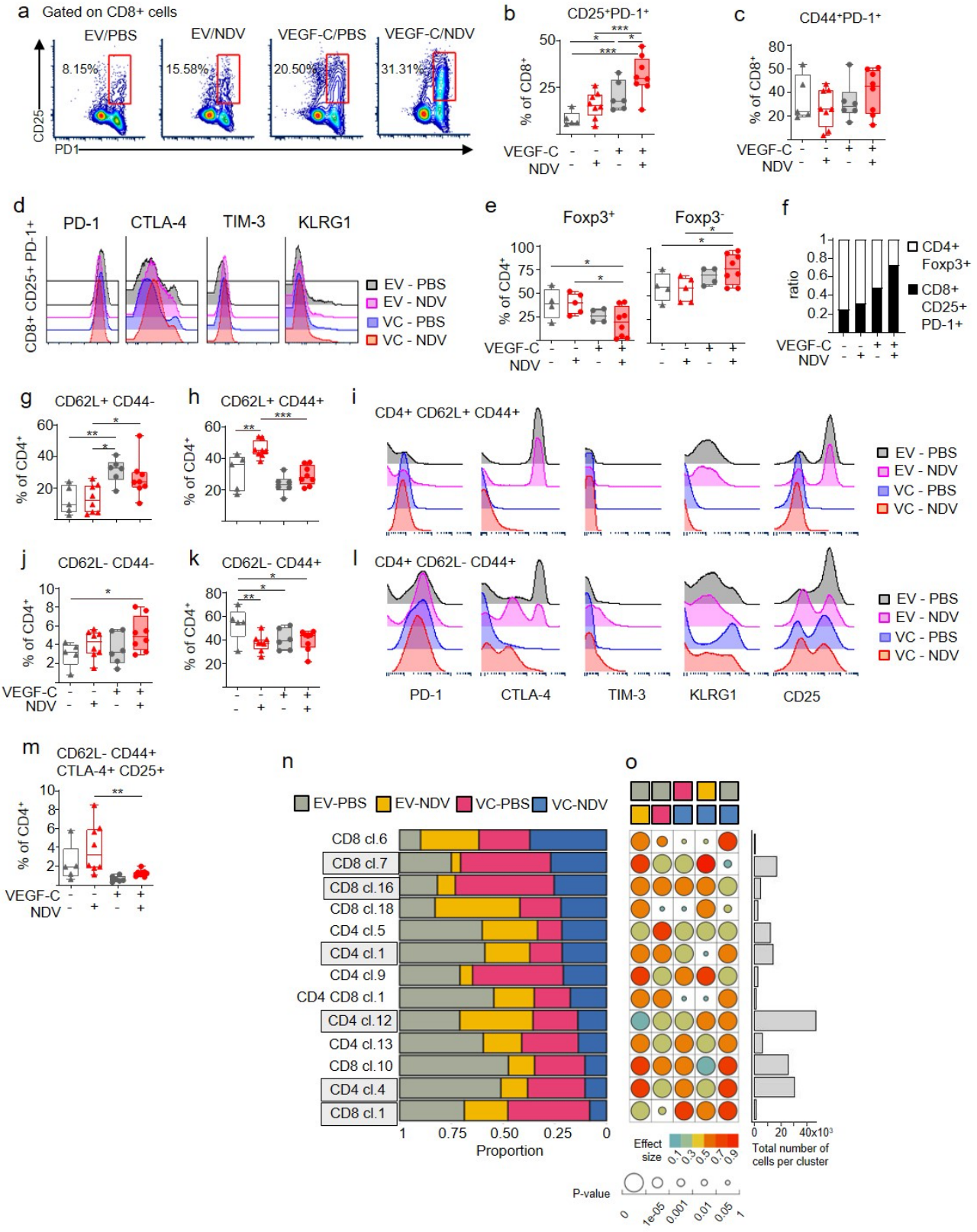
a
Gated on CD8+ cells
EV/PBS
EV/NDV
VEGF-C/PBS
VEGF-C/NDV
8.15%
15.58%
20.50%
31.31%
CD25
PD1
b
CD25+PD-1+
% of CD8+
VEGF-C
NDV
c
CD44+PD-1+
% of CD8+
d
PD-1
CTLA-4
TIM-3
KLRG1
CD8+ CD25+ PD-1+
EV - PBS
EV - NDV
VC - PBS
VC - NDV
e
Foxp3+
Foxp3-
% of CD4+
f
ratio
CD4+ Foxp3+
CD8+ CD25+ PD-1+
g
CD62L+ CD44-
h
CD62L+ CD44+
i
CD4+ CD62L+ CD44+
j
CD62L- CD44-
k
CD62L- CD44+
l
CD4+ CD62L- CD44+
PD-1
CTLA-4
TIM-3
KLRG1
CD25
m
CD62L- CD44+
CTLA-4+ CD25+
n
EV-PBS
EV-NDV
VC-PBS
VC-NDV
CD8 cl.6
CD8 cl.7
CD8 cl.16
CD8 cl.18
CD4 cl.5
CD4 cl.1
CD4 cl.9
CD4 CD8 cl.1
CD4 cl.12
CD4 cl.13
CD8 cl.10
CD4 cl.4
CD8 cl.1
Proportion
o
Effect size
Total number of cells per cluster
P-value

Fig 3. Effects of VEGF-C and NDV on T cell phenotypes. (a-p) Spectral flow cytometry analysis of T-cell subsets in B16/EV and B16/VEGF-C tumors treated as indicated. (a-c) Frequencies of $CD25^{+}PD\text{-}1^{+}$ $CD8^{+}$ T cells; contour plots (a) and Box-and-whiskers plots (b). (c) Frequences of $CD44^{+}PD\text{-}1^{+}$ $CD8^{+}$ T cells. (d) Histograms of checkpoint receptors on $CD25^{+}PD\text{-}1^{+}$ $CD8^{+}$ T cells across treatments. (e) Frequencies of $Foxp3^{+}$ and $Foxp3^{-}$ $CD4^{+}$T cells. (f) Ratios of $CD25^{+}PD\text{-}1^{+}$ CD8 effector T cells to $Foxp3^{+}$ Tregs across treatments as indicated. (g-m) Frequencies of various $CD4^{+}$ T cell subsets (g,h,j,k, m) and histograms for immune check points (i, l) as indicated. Box-and-whiskers plots show individual values with mean ± SEM, and whiskers spanning the full range. EV/PBS, n=5; EV/NDV, n=8; VEGF-C/PBS, n=6; VEGF-C/NDV, n = 8. Statistical analysis with one-way ANOVA multiple comparisons Fisher LSD test. $*p < 0.05$, $**p < 0.01$, $***p < 0.001$, not indicated = not significant. (n) Stacked barplots showing T cell cluster proportions in tumors across treatments. Different experimental groups are represented by their respective colors. Only T cell clusters which showed significant difference between any of the conditions are shown. Most significantly changed T cell clusters are shaded in gray. (o) Heatmap showing p-values (dot size) and effect size (Cohen's W; dot color) of the Chi-square goodness-of-fit test for pairwise comparison of cell cluster proportions across treatments. Only clusters with over 100 cells, medium or large overall effect size and a Chi-square p-value of less than 0.05 in comparisons of different treatments are depicted. The bar plot on the far right displays the total number of cells in each cluster.

Figure 4

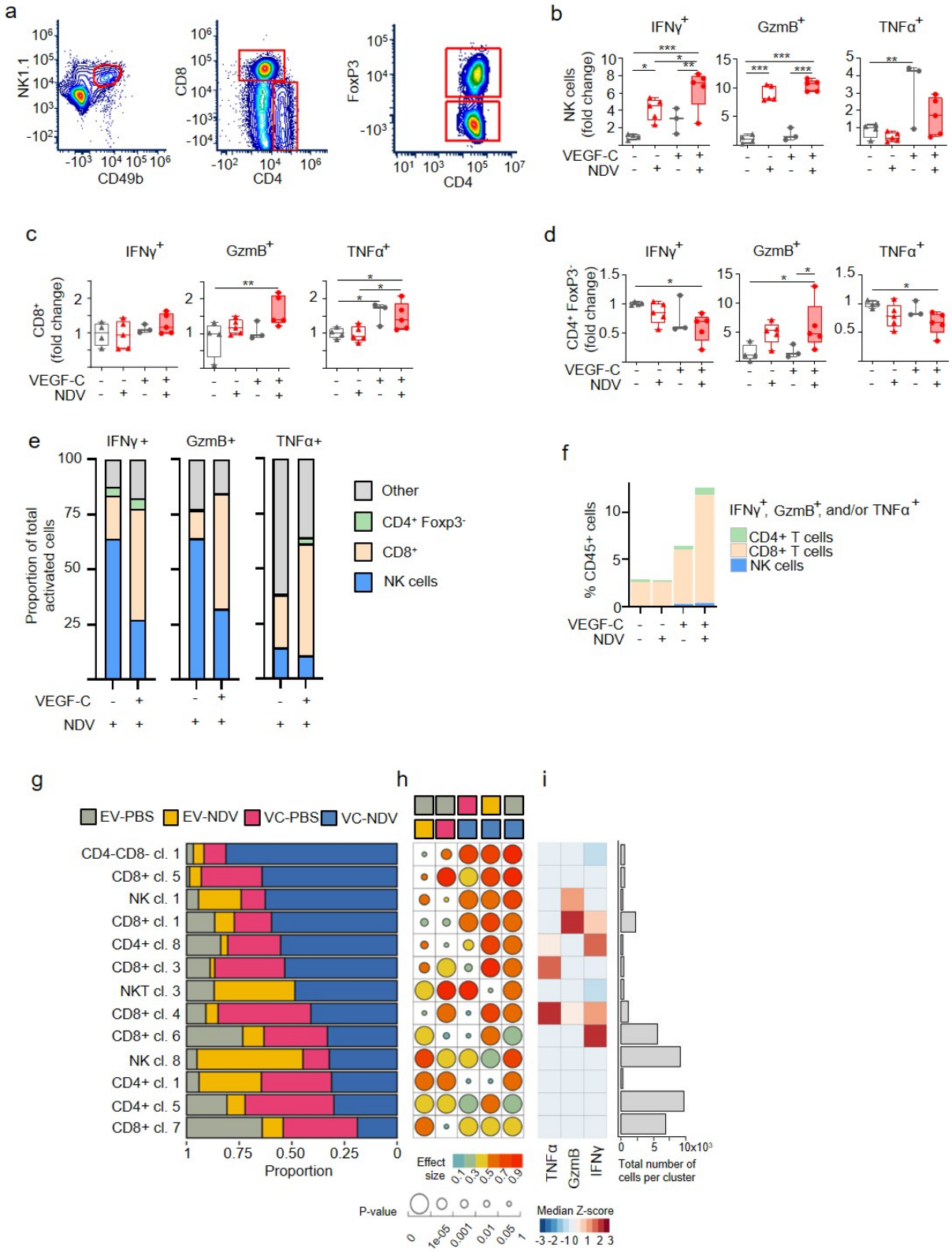
a
NK1.1
CD49b
CD8
CD4
FoxP3
CD4
b
IFNγ+
GzmB+
TNFα+
NK cells (fold change)
VEGF-C
NDV
c
IFNγ+
GzmB+
TNFα+
CD8+ (fold change)
VEGF-C
NDV
d
IFNγ+
GzmB+
TNFα+
CD4+ FoxP3- (fold change)
VEGF-C
NDV
e
IFNγ +
GzmB+
TNFα+
Proportion of total activated cells
Other
CD4+ Foxp3-
CD8+
NK cells
VEGF-C
NDV
f
% CD45+ cells
IFNγ+, GzmB+, and/or TNFα+
CD4+ T cells
CD8+ T cells
NK cells
VEGF-C
NDV
g
EV-PBS
EV-NDV
VC-PBS
VC-NDV
CD4-CD8- cl. 1
CD8+ cl. 5
NK cl. 1
CD8+ cl. 1
CD4+ cl. 8
CD8+ cl. 3
NKT cl. 3
CD8+ cl. 4
CD8+ cl. 6
NK cl. 8
CD4+ cl. 1
CD4+ cl. 5
CD8+ cl. 7
Proportion
h
Effect size
P-value
i
TNFα
GzmB
IFNγ
Total number of cells per cluster
Median Z-score

Fig 4. Effects of VEGF-C and NDV on T cell and NK cell activation in B16F10 tumors. (a-i) Spectral flow cytometry analysis of T cell and NK cell activation. (a) Gating strategy for NK cells, $CD8^+$, $CD4^+$, and $CD4^+$ $Foxp3^+$ T cells. (b-d) Increase or decrease (fold change from EV/PBS control group) of NK cells (b), $CD8^+$ T cells (c), and $CD4^+$ conventional T cells (d), positive for IFNγ, granzyme B (GzmB), or TNFα upon treatments as indicated. Box-and-whiskers plots show individual values with mean ± SEM, and whiskers spanning the full range. EV/PBS, n=4; EV/NDV, n=5; VEGF-C/PBS, n=3; VEGF-C/NDV, n=5. Statistical analysis with one-way ANOVA multiple comparisons Fisher LSD test. (e) Proportion of cells positive for IFNγ, GzmB or TNFα in NDV-treated B16/EV and B16/VEGF-C tumors. (f) Cumulative percentages of activated $CD4^+$ T cells, $CD8^+$ T cells, and NK cells as indicated. (g) Stacked barplots showing cell cluster proportions in tumors across treatments. Different experimental groups are represented by their respective colors. Only T cell clusters which showed significant difference between any of the conditions are shown. (g) Heatmap showing p-values (dot size) and effect size (Cohen's W; dot color) of the Chi-square goodness-of-fit test for pairwise comparisons of cell cluster proportions across treatments. Only clusters with over 100 cells, medium or large overall effect size and a Chi-square p-value of less than 0.05 in comparisons of different treatments are depicted. (i) Heatmap showing the median of z-score normalized mean marker expression values for cell clusters identified based on expression of TNF-α, GrB and/or IFN-γ. The bar plot on the far right displays the total number of cells in each cluster. $*p < 0.05$, $**p < 0.01$, $***p < 0.001$, not indicated = not significant.

Figure 5

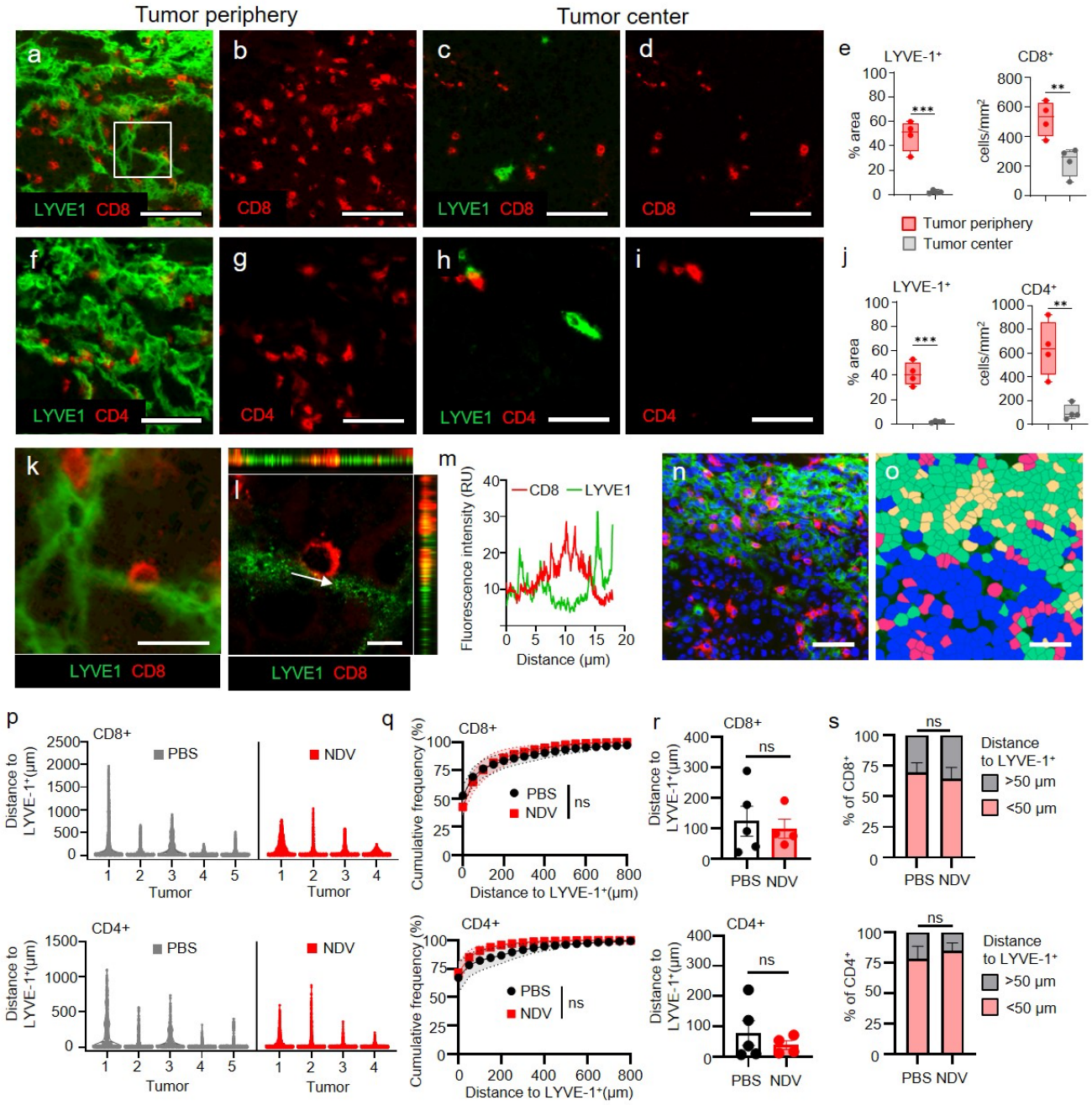

Fig 5. T-cells localize near lymphatic vessels in tumors. (a-d, f-i) NDV-treated B16/VEGF-C tumors immunostained for LYVE-1 (lymphatics, green), and CD8 or CD4, as indicated. Tumor areas with dense and sparse lymphatics are shown. (e, j) Quantification of lymphatic vessel densities and T cells in tumor areas with high and low lymphatic densities, n=4. Box-and-whiskers plots show individual values with

mean ± SEM, and whiskers spanning the full range. (k, l) High magnification image (k) and a z-stack (l) of a boxed area in 5a, showing lymphatic endothelium and $CD8^+$ T cell in close contact. (m) Quantification of the fluorescence intensity in the indicated area, in the direction of the arrow (l). (n, o) Immunofluorescent staining of a representative B16/VEGF-C NDV-treated tumor for $CD8^+$ (red), LYVE-1^+ (green) and DAPI (blue) (n), and a corresponding Qu-Path overlaying mask used for proximity analyses (o). (p-s) Proximity analyses of $CD8^+$ and $CD4^+$ T cells to tumor lymphatics in B16/VEGF-C tumors treated with PBS or NDV. Quantification of the distances from each T cell to the nearest LYVE-1^+ lymphatic vessel (p); Cumulative frequencies of T cells within various distances to the nearest LYVE-1^+ lymphatic vessel. Shaded area indicates STD (q); Average distance of T cells to the nearest LYVE-1^+ vessel (r); T cell frequences within < 50μm or > 50μm of the nearest LYVE-1^+ vessel. Statistical analysis: two-tailed student t-test. $^{**}p < 0.01$, $^{***}p < 0.001$, ns = not significant. Scale bars: a-d, f-i: 100 μm; k: 25 μm, l: 10 μm; n, o: 50 μm.

Figure 6

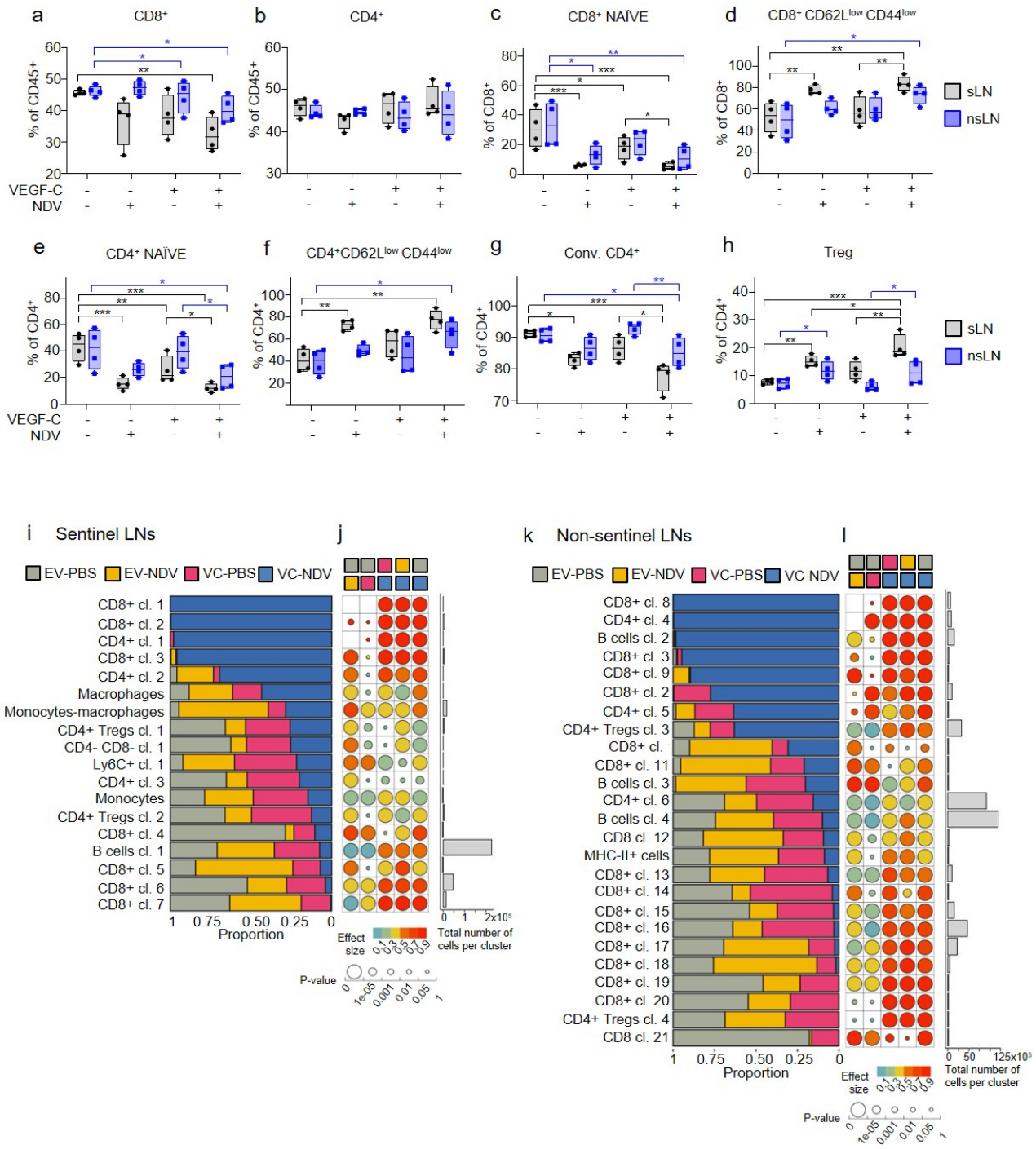

Fig 6. Effects of VEGF-C and NDV on immune cell composition in the lymph nodes of B16F10 tumor-bearing mice. (a-h) Spectral flow cytometry analysis of T cells in sLNs and non-sLNs. Relative

frequences of distinct $CD8^+$ and $CD4^+$ T cell subsets are shown; total $CD8^+$ (a), total $CD4^+$ (b), naïve $CD8^+$ T cells (c), $CD8^+$ $CD62L^{low}$ $CD44^{low}$ T cells (d), naïve $CD4^+$ T cells (e), $CD4^+$ $CD62L^{low}CD44^{low}$ T cells (f), $CD4^+$ Tconv (g), $CD4^+$ $Foxp3^+$ Tregs (h). Statistical analysis: one-way ANOVA multiple comparisons. n=4. Box-and-whiskers plots show individual values with mean ± SEM, and whiskers spanning the full range. (i,k) Stacked barplots showing cell cluster proportions in sentinel LNs (i) and non-sentinel LNs (k) across treatments. Different experimental groups are represented by their respective colors. Only cell clusters which showed significant difference between any of the conditions are shown (j, l) Heatmap shows p-values (dot size) and effect size (Cohen's W; dot color) of the Chi-square goodness-of-fit test for pairwise comparison of cell cluster proportions across treatments. Only clusters with over 100 cells, medium or large overall effect size and a Chi-square p-value of less than 0.05 in comparisons of different treatments are depicted. The bar plot on the far right displays the total number of cells in each cluster. *$p < 0.05$, **$p < 0.01$, ***$p < 0.001$, not indicated = not significant.

Figure 7

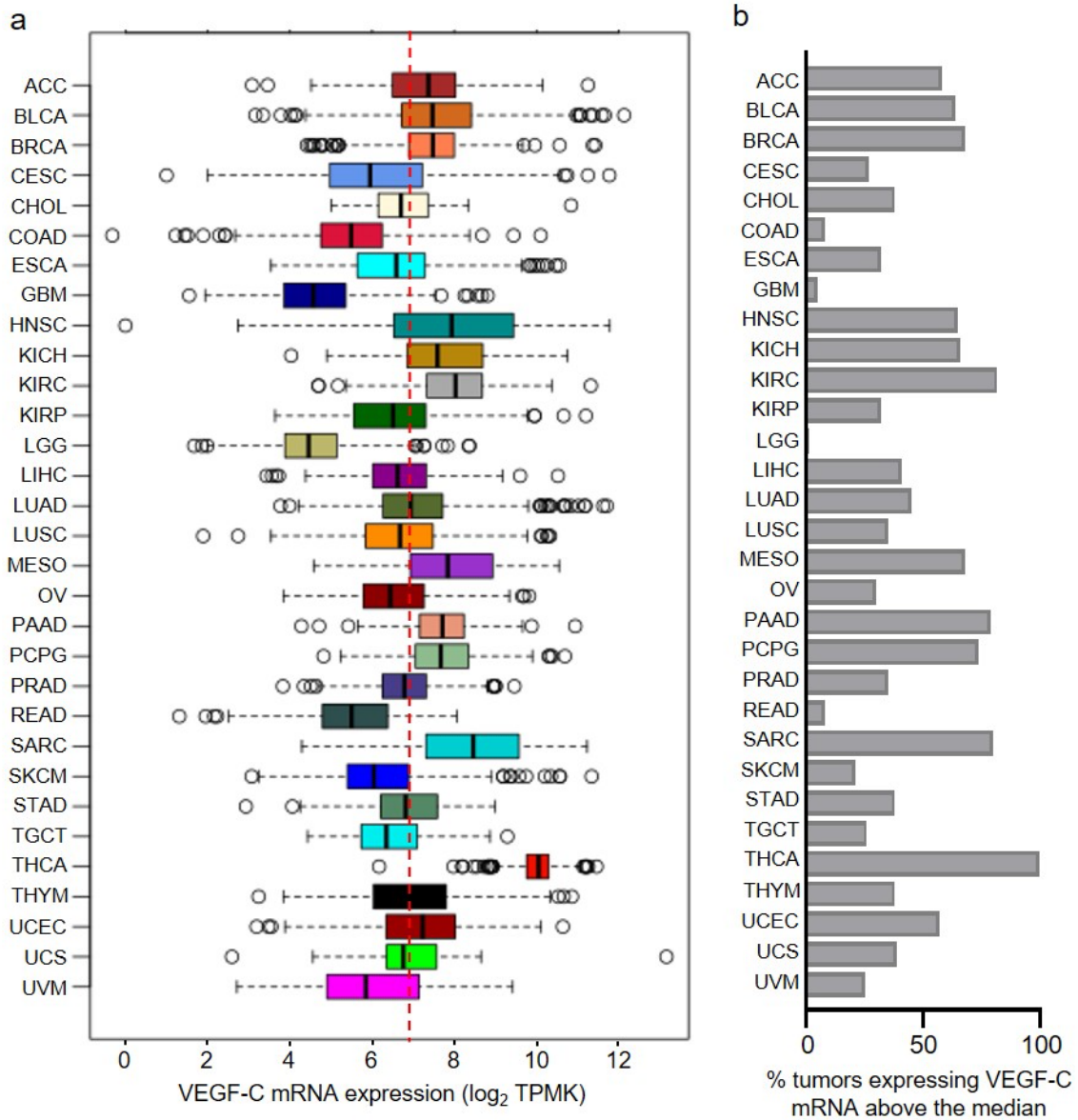

Fig 7. VEGF-C mRNA expression in human tumors. (a) Gene expression data from the TCGA PANCAN 2022 cohort showing expression of VEGF-C in human solid tumors (n=10,839). The red dotted line indicates median VEGF-C expression across all solid tumors in the cohort. (b) Percentage of tumors within each cancer type expressing VEGF-C above the pan-cancer median. Tumor type abbreviations follow The Cancer Genome Atlas (TCGA) nomenclature: ACC (Adrenocortical carcinoma), BLCA

(Bladder urothelial carcinoma), BRCA (Breast invasive carcinoma), CESC (Cervical squamous cell carcinoma and endocervical adenocarcinoma), CHOL (Cholangiocarcinoma), COAD (Colon adenocarcinoma), ESCA (Esophageal carcinoma), GBM (Glioblastoma multiforme), HNSC (Head and neck squamous cell carcinoma), KICH (Kidney chromophobe), KIRC (Kidney renal clear cell carcinoma), KIRP (Kidney renal papillary cell carcinoma), LGG (Low-grade glioma), LIHC (Liver hepatocellular carcinoma), LUAD (Lung adenocarcinoma), LUSC (Lung squamous cell carcinoma), MESO (Mesothelioma), OV (Ovarian serous cystadenocarcinoma), PAAD (Pancreatic adenocarcinoma), PCPG (Pheochromocytoma and paraganglioma), PRAD (Prostate adenocarcinoma), READ (Rectum adenocarcinoma), SARC (Sarcoma), SKCM (Skin cutaneous melanoma), STAD (Stomach adenocarcinoma), TGCT (Testicular germ cell tumors), THCA (Thyroid carcinoma), THYM (Thymoma), UCEC (Endometrial cancer), UCS (Uterine carcinosarcoma), and UVM (Uveal melanoma).

Table 1. Complete response rates upon treatment of B16/EV or B16/VEGF-C tumors with NDV or APMV4. Number of tumor-free surviving mice over total number of mice in an experiment is indicated. Data are shown from ten independent experiments. CR, complete response.

	PBS		NDV		rechallenge	APMV4		rechallenge
Exp #	EV	VEGF-C	EV	VEGF-C	EV	EV	VEGF-C	EV
1	0/9	0/8	0/10	6/10	2/6	0/10	7/9	4/6
2	0/7	0/7	1/7	6/7	5/6	0/7	7/7	5/7
3	0/8		0/10					
4	0/7		0/7					
5							9/9	
6							2/5	
7							4/4	
8							5/5	
9							3/5	
10							5/5	
CR	**0/31**	**0/15**	**1/34**	**12/17**	**7/12**	**0/17**	**42/49**	**9/13**
%CR	**0%**	**0%**	**3%**	**71%**	**58%**	**0%**	**86%**	**69%**

Table 2. Cumulative incidence of lymph node metastasis. Number of mice with sentinel LNs positive for metastasis. Each mouse had one tumor and one sentinel lymph node.

	PBS	APMV4	
Exp #	VEGF-C		Days after treatment
1	10/10		
2	8/8		
3		0/4	120
4		0/5	454
5		0/5	843
6		0/9	751
# LN w mets	**18/18**	**0/23**	
% LN w mets	**100%**	**0%**	

Table 3. Markers used in spectral flow cytometry

Panel 1: Tumor Myeloid and lymphoid Cell surface	**Panel 2: Tumor** Lymphoid Cell surface	**Panel 3: Tumor** Lymphoid Intracellular	**Panel 4: Lymph Nodes** Myeloid and lymphoid Cell surface
B220	CD62L	B220	B220
CCR2	CD25	CD3	CD103
CD103	CD28	CD4	CD11b
CD11b	CD3	CD45	CD11c
CD11c	CD4	CD49b	CD3
CD45	CD44	CD8	CD44
CD49b	CD45	Foxp3	CD45
CD64	CD49b	GrzmB	CD49b
CD8	CD8	IFNγ	CD62L
CD80	CTLA-4	Live Dead	CD64
CD83	CXCR3	NK1.1	CD8
CD86	KLRG1	TNFα	CD83
F4/80	Live Dead		CD86
Live Dead	PD-1		Foxp3
Ly6C	TIM-3		Live Dead
Ly6G			Ly6C
MHCII			Ly6G
PD-L1			MHCII
			PD-L1